

Enhancing classical simulation with noisy quantum devices

Ruiqi Zhang^{1, 2} Fuchuan Wei^{1, 2} and Zhaohui Wei^{1, 3, *}

¹Yau Mathematical Sciences Center, Tsinghua University, Beijing 100084, China

²Department of Mathematics, Tsinghua University, Beijing 100084, China

³Yanqi Lake Beijing Institute of Mathematical Sciences and Applications, Beijing 100407, China

As quantum devices continue to improve in scale and precision, a central challenge is how to effectively utilize noisy hardware for meaningful computation. Most existing approaches aim to recover noiseless circuit outputs from noisy ones through error mitigation or correction. Here, we show that noisy quantum devices can be directly leveraged as computational resources to enhance the classical simulation of quantum circuits. We introduce the *Noisy-device-enhanced Classical Simulation* (NDE-CS) protocol, which improves stabilizer-based classical Monte Carlo simulation methods by incorporating data obtained from noisy quantum hardware. Specifically, NDE-CS uses noisy executions of a target circuit together with noisy Clifford circuits to learn how the target circuit can be expressed in terms of Clifford circuits under realistic noise. The same learned relation can then be reused in the noiseless Clifford limit, enabling accurate estimation of ideal expectation values with substantially reduced sampling cost. Numerical simulations on Trotterized Ising circuits demonstrate that NDE-CS achieves orders-of-magnitude reductions in sampling cost compared to the underlying purely classical Monte Carlo approaches from which it is derived, while maintaining the same accuracy. We also compare NDE-CS with Sparse Pauli Dynamics (SPD), a powerful classical framework capable of simulating quantum circuits at previously inaccessible scales, and provide an example where the cost of SPD scales exponentially with system size, while NDE-CS scales much more favorably. These results establish NDE-CS as a scalable hybrid simulation approach for quantum circuits, where noise can be harnessed as a computational asset.

I. INTRODUCTION

Quantum computing is approaching a pivotal milestone where its advantages over classical computation may soon be demonstrated across a range of practical tasks [1–4]. Nevertheless, noise remains an intrinsic feature of current quantum devices, posing a major obstacle to their reliable operations and large-scale deployments [5–9]. Most near-term quantum algorithms depend on obtaining accurate, effectively noiseless expectation values to yield meaningful results [10–14]. Because quantum error correction remains prohibitively expensive, a broad spectrum of quantum error mitigation (QEM) techniques has been developed to address the detrimental effects of hardware noise [10, 11, 15–19]. Although QEM can recover high-fidelity observables for small systems, its reliance on repeated circuit executions, extrapolation, and probabilistic rescaling leads to significant computational overhead, making large-scale applications increasingly impractical as circuit size and depth grow.

These limitations motivate a natural and fundamental question. *Can noisy quantum devices be directly employed as computational resources to assist in solving classically hard problems, rather than being corrected or mitigated?* In this paper, we will show that a possible avenue toward this goal is to use noisy quantum data to enhance the classical simulation of quantum circuits, thus transforming unavoidable hardware noise into a constructive element of computation.

Classical simulation of quantum circuits plays a central role in understanding quantum many-body dynamics and solving practical problems in physics and chemistry. Beyond validating quantum processors, it enables the study of quantum evolution and correlations that are difficult to access analytically. Various simulation frameworks, including tensor-network contraction [20, 21], stabilizer-rank and quasiprobability decomposition [22–27], have been developed to approximate the behavior of non-Clifford quantum circuits. Existing stabilizer-based simulation approaches for simulating non-Clifford quantum circuits typically rely on expressing the target parameterized quantum circuit (PQC) as a linear combination of classically efficiently simulable circuits [23]. However, for generic non-Clifford circuits, this strategy incurs a fundamental limitation: both the number of terms in the decomposition and the ℓ_1 -norm of the associated coefficients typically grow exponentially with the number of non-Clifford gates. As a consequence, the sampling cost required to achieve a fixed target precision scales exponentially with circuit depth, limiting the applicability of these methods to large and deep circuits.

In this work, we leverage noisy quantum devices to reduce the simulation cost of stabilizer-based classical simulation methods. To address these challenges in stabilizer-based approaches, we first introduce a structure-aware simulation framework, termed structure-preserving Monte Carlo (SPMC), which decomposes a PQC into a linear combination of Clifford circuits that preserve the original circuit architecture. Although SPMC does not reduce the number of terms required in the decomposition, it enforces that all sampled Clifford circuits retain the same gate layout and connectivity as

* weizhaohui@gmail.com

the target circuit. As a result, the sampled circuits exhibit hardware-specific noise characteristics that closely match those of the target PQC [28, 29], thereby providing a natural interface between classical simulation and realistic quantum devices.

Building on SPMC, we develop the Noisy-device-enhanced Classical Simulation (NDE-CS) protocol, which exploits this interface to further reduce the simulation cost. Rather than relying on the full noiseless Clifford decomposition of the target PQC, NDE-CS leverages the noisy realizations of both the target circuit and its associated Clifford circuits executed on quantum hardware to identify an effective representation involving substantially fewer terms in the presence of noise. By incorporating randomized Pauli insertions, the learned noisy decomposition remains valid for the estimation of observables of the noiseless target circuit. As a result, the Clifford decomposition learned from noisy circuit executions can be applied to noiseless Clifford circuits, enabling the estimation of expectation values of the noiseless target circuit using only classically simulable data.

Numerical simulations demonstrate that NDE-CS achieves orders-of-magnitude improvements over purely classical Monte Carlo approaches. For example, for a 16-qubit Trotterized Ising circuit, Static and Dynamic Monte Carlo methods [23] require an estimated $\sim 10^{41}$ samples to reach a relative error of 10^{-2} , whereas NDE-CS attains comparable accuracy using only $\sim 10^5$ noisy circuit executions. More broadly, across 10-14 qubit Trotter circuits, we observe that while the cost of Static and Dynamic Monte Carlo grows rapidly with both circuit depth and qubit number, the sampling cost of NDE-CS exhibits a markedly weaker dependence on the system size. Moreover, as the Trotter step number increases, the performance gap between NDE-CS and Static and Dynamic Monte Carlo methods becomes more pronounced. These results establish NDE-CS as a scalable hybrid quantum-classical simulation paradigm whose relative advantage becomes increasingly pronounced as quantum circuits grow larger and deeper.

In addition to Monte Carlo-based stabilizer methods, we compare NDE-CS with Sparse Pauli Dynamics (SPD), a powerful path-based classical simulation approach that has recently enabled accurate simulations of quantum circuits at system sizes that were previously difficult to access classically. By constructing a structured family of circuits, we identify a regime in which the computational cost of SPD grows exponentially with system size, while NDE-CS attains accurate estimates with a sampling cost that depends only weakly on the number of qubits. This comparison highlights a complementary regime in which access to noisy quantum hardware allows NDE-CS to provide a clear practical advantage over purely classical path-based simulation methods.

The remainder of this paper is organized as follows. Section II introduces the basic notations and circuit models used throughout this work, together with a brief review of quasiprobability sampling and stabilizer-based

simulation methods. Section III introduces the SPMC method as the theoretical foundation of our work. Section IV presents the NDE-CS protocol and its theoretical guarantees. Section V reports numerical results for Trotterized Ising circuits under Pauli noise and compares NDE-CS with other classical simulation methods. Finally, Section VI summarizes our findings and discusses potential extensions of the proposed framework.

II. PRELIMINARIES

In this section, we present the circuit and noise models considered in this work, followed by a brief overview of several known classical simulation techniques based on quasiprobability and stabilizer methods.

A. Circuit Model and Noise Model

In the NISQ era, parameterized quantum circuits (PQCs) are widely employed in various near-term quantum algorithms [30, 31]. A typical n -qubit PQC, denoted by $C(\theta)$, consists of a sequence of Pauli rotation gates and non-parameterized Clifford gates. Each Pauli rotation gate is written as $e^{-i\frac{\theta}{2}P}$, where θ is the rotation angle and $P \in \{I, X, Y, Z\}^{\otimes n}$ is an n -qubit Pauli operator. Clifford gates are unitary operators that normalize the n -qubit Pauli group \mathcal{P}_n :

$$\{C \in \mathcal{U}_{2^n} \mid C\mathcal{P}_nC^\dagger = \mathcal{P}_n\}.$$

Without loss of generality, we assume that a PQC takes the form

$$C(\theta) = U_L(\theta_L) \cdots U_1(\theta_1), \quad (1)$$

where $\theta = (\theta_1, \dots, \theta_L)$ are the rotation angles and L is the circuit depth. Each unitary $U_l(\theta_l)$ is of the form

$$U_l(\theta_l) := e^{-i\theta_l P_l/2} C_l,$$

where $P_l \in \{I, X, Y, Z\}^{\otimes n}$ and C_l is a Clifford gate.

To describe noise, we adopt the channel representation. For a unitary U , we denote the corresponding quantum channel by $\mathcal{U}(\rho) = U\rho U^\dagger$. Let $\mathcal{U}_l(\theta_l)$ be the channel associated with $U_l(\theta_l)$. The overall noiseless circuit channel is then

$$\mathcal{C}(\theta) = \mathcal{U}_L(\theta_L) \circ \cdots \circ \mathcal{U}_1(\theta_1). \quad (2)$$

Acting on an initial state ρ , we evaluate the observable expectation value as

$$\langle O \rangle = \text{Tr}(O \mathcal{C}(\theta)(\rho)).$$

In realistic quantum devices, each unitary $\mathcal{U}_l(\theta_l)$ is implemented imperfectly. We represent the noisy implementation by a quantum channel $\tilde{\mathcal{U}}_l(\theta_l)$, which we model as

$$\tilde{\mathcal{U}}_l(\theta_l) = \mathcal{E}_l \circ \mathcal{U}_l(\theta_l), \quad (3)$$

where \mathcal{E}_l is a noise channel. The resulting noisy circuit becomes

$$\tilde{\mathcal{C}}(\boldsymbol{\theta}) = \tilde{\mathcal{U}}_L(\theta_L) \circ \cdots \circ \tilde{\mathcal{U}}_1(\theta_1) = \mathcal{E}_L \circ \mathcal{U}_L(\theta_L) \circ \cdots \circ \mathcal{E}_1 \circ \mathcal{U}_1(\theta_1),$$

with noisy expectation value

$$\langle O_{\text{noisy}} \rangle = \text{Tr} \left(O \tilde{\mathcal{C}}(\boldsymbol{\theta})(\rho) \right).$$

Throughout this work, we focus on Pauli noise, as general noise processes can be mapped to Pauli channels via Pauli twirling [10, 11, 32–36]. Motivated by the noise characteristics observed in current quantum hardware [10, 11], we consider the following Pauli noise model:

$$\mathcal{E}(\rho) = \bigcirc_{k \in \mathcal{K}} \left(w_k \cdot + (1 - w_k) P_k \cdot P_k^\dagger \right) (\rho), \quad (4)$$

where \bigcirc denotes the sequential composition of single-Pauli channels.

For each parameterized gate $U_l(\theta_l) = e^{-i\theta_l/2} P_l C_l$ with $l = 1, 2, \dots, L$, we additionally consider a Pauli noise channel aligned with its rotation axis:

$$\mathcal{E}_{P_l}(\rho) = (1 - \gamma_l) \rho + \gamma_l P_l \rho P_l^\dagger, \quad (5)$$

where γ_l is the single-gate noise rate and the Pauli operator P_l is the generator of the rotation.

B. Monte Carlo and Stabilizer-Based Methods for Quantum Circuit Simulation

Stabilizer circuits, consisting of Clifford operations acting on stabilizer states, can be simulated efficiently on a classical computer by the Gottesman–Knill theorem [37]. Once non-stabilizer (“magic”) operations are introduced, the resulting circuits may become universal for quantum computing, and their classical simulation cost generally grows exponentially with the amount of magic [38]. Building on the stabilizer framework, two major extensions have been developed to simulate circuits containing non-stabilizer components: quasiprobability-based Monte Carlo methods [23, 25, 26, 39–41] and stabilizer-rank approaches [22, 42–44]. In both families, the classical cost is controlled by a magic monotone that quantifies the deviation from the stabilizer region.

Among these extensions, quasiprobability Monte Carlo methods align most naturally with our channel-based perspective. Their central idea is to express a general quantum channel as a signed linear combination of channels that can be simulated efficiently using stabilizer techniques. Once such a decomposition is available, one samples from the associated quasiprobability distribution and evaluates stabilizer trajectories, obtaining an unbiased estimator for the target computational output. This reduces the simulation of a non-Clifford circuit to repeated simulations of efficiently tractable components.

There exist multiple approaches for efficiently simulating quantum circuits. Earlier work explored decompositions over Clifford gates supplemented by Pauli

reset channels [25]. This class is strictly contained within the more general class of completely stabilizer-preserving (CSP) maps, which form the broadest set of operations that preserve stabilizer structure [23, 41, 45]. Using CSP maps yields the most general formulation of quasiprobability Monte Carlo and accommodates a wide range of gate and noise models. Below, we summarize this general formulation, commonly referred to as Static Monte Carlo [23].

The Static Monte Carlo (SMC) method represents an n -qubit channel \mathcal{E} as

$$\mathcal{E}(\rho) = \sum_k q_k \mathcal{S}_k(\rho), \quad \sum_k q_k = 1, \quad (6)$$

where each \mathcal{S}_k is a CSP map (formal definitions are provided in Suppl. Mat. I). The coefficients $\{q_k\}$ may be negative, and their signs encode the non-stabilizing character of \mathcal{E} . Since CSP maps admit efficient stabilizer simulation, Eq. (6) enables one to reduce the evaluation of $\mathcal{E}(\rho)$ to repeated stabilizer computations. The explicit sampling procedure is described below.

To estimate the expectation value $\langle O \rangle = \text{Tr}(O \mathcal{E}(\rho))$ of an observable O —assumed to be a polynomial-size linear combination of Pauli operators—on an input stabilizer state ρ , one samples indices k according to the normalized quasiprobability distribution

$$p_k = \frac{|q_k|}{\sum_j |q_j|}, \quad (7)$$

and computes $\mathcal{S}_k(\rho)$, which remains a stabilizer state. Each sample contributes $s_k \text{Tr}(O \mathcal{S}_k(\rho))$ with $s_k = \text{sign}(q_k)$. After M samples, the value of the estimator is

$$\hat{O} = \frac{\sum_j |q_j|}{M} \sum_{i=1}^M s_{k_i} \text{Tr}(O \mathcal{S}_{k_i}(\rho)), \quad (8)$$

which is unbiased for $\langle O \rangle$. The variance scales as $\text{Var}(\hat{O}) \sim (\sum_j |q_j|)^2/M$, indicating that the simulation cost is determined by the squared ℓ_1 -norm of the coefficients $\{q_k\}$ which decompose the channel \mathcal{E} .

Minimizing this cost yields the channel robustness

$$\mathcal{R}_*(\mathcal{E}) = \min_{\{q_k, \mathcal{S}_k\}} \sum_k |q_k|, \quad (9)$$

which equals 1 precisely when \mathcal{E} is CSP and is strictly larger otherwise.

For a circuit composed of multiple layers and written as

$$\mathcal{E} = \mathcal{E}_L \circ \cdots \circ \mathcal{E}_1, \quad (10)$$

each layer \mathcal{E}_i can be decomposed independently, and the Monte Carlo sampler draws a stabilizer-preserving map from each layer in sequence. The resulting stabilizer trajectory yields an unbiased estimator with variance

$\text{Var}(\hat{O}) \sim \prod_{l=1}^L \mathcal{R}_*(\mathcal{E}_l)^2/M$, leading to a total simulation cost on the order of $\mathcal{O}\left(\prod_{l=1}^L \mathcal{R}_*(\mathcal{E}_l)^2\right)$. Additional technical details on the multi-layer composition can be seen in Suppl. Mat. I.

Ref. [23] also introduced a local and adaptive variant termed Dynamic Monte Carlo (DMC), in which quasiprobabilities for each intermediate decomposition will depend on the stabilizer state sampled in the previous step. The associated simulation cost is governed by the magic capacity of the channel $\mathcal{C}(\mathcal{E})$ [23],

$$\mathcal{C}(\mathcal{E}) = \max_{|\phi\rangle \in \text{STAB}_{2n}} \mathcal{R}[(\mathcal{E} \otimes \mathcal{I}_n) |\phi\rangle\langle\phi|], \quad (11)$$

with \mathcal{I}_n being the identity channel on an n -qubit Hilbert space, and \mathcal{R} is the robustness of magic of a quantum state. It can be seen that $\mathcal{C}(\mathcal{E}) \leq \mathcal{R}_*(\mathcal{E})$, i.e., the simulation cost of DMC is no greater than that of SMC.

III. STRUCTURE-PRESERVING MONTE CARLO SIMULATION

The SMC method provides a general quasiprobability-based framework for circuit simulation. However, for a deep PQC, obtaining a CSP decomposition of the entire circuit that minimizes the total ℓ_1 -norm of the decomposed coefficients is generally infeasible. As a consequence, the associated sampling complexity typically grows exponentially with circuit depth. In this section, we introduce the structure-preserving Monte Carlo (SPMC) method to address this challenge, which decomposes a target PQC into an ensemble of Clifford circuits that can be efficiently simulated classically. Specifically, in SPMC, each non-Clifford channel in the target circuit is decomposed into a linear combination of Clifford circuit channels that preserve the architecture of the target PQC. In other words, all sampled Clifford circuits are composed of a similar sequence of Clifford gates, differing only in discrete Clifford-compatible rotation angles. This enables the faithful emulation of the corresponding noise behavior for these quantum circuits on superconducting hardware [28, 29]. Crucially, in the next section, we will see that this feature allows us to leverage noisy quantum hardware to substantially reduce the overall simulation cost.

A. Decomposition of parameterized quantum circuits

In this subsection, we present a decomposition of the quantum channel associated with a PQC into a linear combination of Clifford circuit channels. The objective is to construct such a decomposition with the ℓ_1 -norm of the coefficients kept as small as possible, since this quantity directly determines the sample complexity of the Monte Carlo estimator.

Consider a general parameterized quantum circuit channel defined in Eq. (2)

$$\mathcal{C}(\boldsymbol{\theta}) = \mathcal{U}_L(\theta_L) \circ \dots \circ \mathcal{U}_1(\theta_1), \quad (12)$$

where $\mathcal{U}_l(\theta_l) := e^{-i\theta_l P_l/2} C_l$. Since C_l itself is Clifford, it suffices to decompose only the rotation part $e^{-i\theta_l P_l/2}$ into a linear combination of Clifford rotations.

For angles $\theta \in [0, \pi/4]$, Ref. [25] provides a decomposition of $\mathcal{R}_Z(\theta)$ into only three Clifford channels, and the resulting ℓ_1 -norm is provably minimal.

Lemma 1 ([25]). *For the channel $\mathcal{R}_Z(\theta)$ corresponding to the rotation gate $R_Z(\theta)$, one has the decomposition*

$$\mathcal{R}_Z(\theta) = \frac{1 + \cos \theta - \sin \theta}{2} \mathcal{I} + \frac{1 - \cos \theta - \sin \theta}{2} \mathcal{Z} + \sin \theta \mathcal{S},$$

where $\mathcal{I}, \mathcal{Z}, \mathcal{S}$ denote the channels associated with the gates I , Z , and S , respectively. For $\theta \in [0, \pi/4]$, this decomposition achieves the minimal possible ℓ_1 -norm among all exact decompositions.

We now present an alternative Clifford decomposition that applies to all $\theta \in [0, 2\pi]$, and furthermore, it generalizes naturally to an arbitrary n -qubit Pauli rotation channel. Moreover, as discussed later in our treatment of noisy circuits, this decomposition is particularly advantageous when the rotation gate is followed by axis-aligned Pauli noise, since the combined noisy gate admits an even more favorable ℓ_1 -norm under our approach.

Lemma 2 (Optimal Clifford decomposition of rotation gate). *For any single-parameter rotation gate $e^{-i\theta P/2}$ generated by a Pauli operator $P \in \{I, X, Y, Z\}^{\otimes n}$, let $\mathcal{R}_P(\theta)$ denote the corresponding quantum channel representation. Then, the minimal ℓ_1 -norm of the Clifford decomposition coefficients satisfies*

$$\min_{a_i, \mathcal{C}_i} \left\{ \sum_i |a_i| : \sum_i a_i \mathcal{C}_i = \mathcal{R}_P(\theta) \right\} = |\sin(\theta)| + |\cos(\theta)|,$$

where each \mathcal{C}_i is a Clifford circuit channel. Furthermore, we have

$$\mathcal{R}_P(\theta) = \sum_{k=0}^3 a_k \mathcal{R}_P(k\pi/2),$$

where

$$a_0 = \frac{|\cos \theta|}{2(|\sin \theta| + |\cos \theta|)} + \frac{\cos \theta}{2}, \quad a_2 = \frac{|\cos \theta|}{2(|\sin \theta| + |\cos \theta|)} - \frac{\cos \theta}{2},$$

$$a_1 = \frac{|\sin \theta|}{2(|\sin \theta| + |\cos \theta|)} + \frac{\sin \theta}{2}, \quad a_3 = \frac{|\sin \theta|}{2(|\sin \theta| + |\cos \theta|)} - \frac{\sin \theta}{2},$$

and $\sum_{k=0}^3 |a_k| = |\sin(\theta)| + |\cos(\theta)|$.

The above lemma establishes that the minimal ℓ_1 -norm of the Clifford decomposition coefficients for any n qubit Pauli rotation channel $\mathcal{R}_P(\theta)$ is given by $|\sin(\theta)| + |\cos(\theta)|$. In other words, to obtain the most efficient linear decomposition, it is sufficient to represent

$\mathcal{R}_P(\theta)$ using only the four Clifford-equivalent channels $\{\mathcal{R}_P(k\pi/2)\}_{k=0}^3$, which achieves the smallest attainable ℓ_1 -norm among all possible Clifford decompositions, and hence reduces the Monte Carlo sampling overhead in the simulation. The proof of Lemma 2 is provided in Suppl. Mat. II.

If each non-Clifford rotation gate in the circuit $\mathcal{C}(\theta)$ is decomposed using Lemma 2, then for gate $\mathcal{U}_l(\theta_l) = \mathcal{R}_{P_l}(\theta_l) \circ \mathcal{C}_l$ can be decomposed into $\mathcal{U}_l(k\pi/2) = \mathcal{R}_{P_l}(k\pi/2) \circ \mathcal{C}_l$ with the same coefficients $a_k, k = 0, 1, 2, 3$ to decompose $\mathcal{R}_{P_l}(\theta_l)$, and the entire non-Clifford circuit can be expressed as a linear combination of Clifford circuits:

$$\begin{aligned} \mathcal{C}(\theta) &= \mathcal{U}_L(\theta_L) \circ \cdots \circ \mathcal{U}_1(\theta_1) \\ &= \left(\sum_{k_L=0}^3 a_{k_L}^{(L)} \mathcal{U}_L\left(\frac{k_L\pi}{2}\right) \right) \circ \cdots \left(\sum_{k_1=0}^3 a_{k_1}^{(1)} \mathcal{U}_1\left(\frac{k_1\pi}{2}\right) \right) \\ &= \sum_{k_1, \dots, k_L} a_{k_1}^{(1)} \cdots a_{k_L}^{(L)} \mathcal{U}_L\left(\frac{k_L\pi}{2}\right) \circ \cdots \circ \mathcal{U}_1\left(\frac{k_1\pi}{2}\right). \end{aligned} \quad (13)$$

All the Clifford circuits appearing in this expansion retain the exact same gate sequence and connectivity as the original variational circuit, differing only in the discrete rotation angles $\{k_l\pi/2\}$. The coefficients $a_{k_l}^{(l)}$ are defined in Lemma 2 for each layer l , and this decomposition achieves the minimal ℓ_1 -norm if each non-Clifford

rotation gate is individually decomposed.

B. Structure-preserving Monte Carlo sampling

Based on the Clifford decomposition above, we next describe how the quasiprobability sampling is performed in the structure-preserving framework. Consider a parameterized circuit channel $\mathcal{C}(\theta) = \mathcal{U}_L(\theta_L) \circ \cdots \circ \mathcal{U}_1(\theta_1)$. For the l -th layer, we denote the decomposition coefficients by $\{a_{k_l}^{(l)}\}$, with $\sum_{k_l} a_{k_l}^{(l)} \mathcal{U}_l(k_l\pi/2) = \mathcal{U}_l(\theta_l)$ and $\sum_{k_l} |a_{k_l}^{(l)}| = |\sin(\theta_l)| + |\cos(\theta_l)|$, same as in Eq. (13).

In the SPMC algorithm, the circuit is sampled layer by layer. At each layer l , a Clifford channel $\mathcal{U}_l(k_l\pi/2)$ is drawn according to the normalized quasiprobability

$$p_{k_l}^{(l)} = \frac{|a_{k_l}^{(l)}|}{|\sin(\theta_l)| + |\cos(\theta_l)|}, \quad s_{k_l}^{(l)} = \text{sign}(a_{k_l}^{(l)}), \quad (14)$$

and the sequence $\vec{k} = (k_1, \dots, k_L)$ forms a sampled *trajectory*. Each trajectory corresponds to a Clifford circuit that preserves the full architecture of the original variational circuit, differing only in the discrete rotation angles. The expectation value of an observable O is then estimated by averaging over M sampled trajectories as

$$\hat{O} = \frac{\prod_{l=1}^L (|\sin(\theta_l)| + |\cos(\theta_l)|)}{M} \sum_{i=1}^M \left(\prod_{l=1}^L s_{k_l^{(i)}}^{(l)} \right) \text{Tr} \left[O \mathcal{U}_L\left(\frac{k_L^{(i)}\pi}{2}\right) \circ \cdots \circ \mathcal{U}_1\left(\frac{k_1^{(i)}\pi}{2}\right)(\rho) \right]. \quad (15)$$

This estimator is unbiased, and its variance scales as $\text{Var}(\hat{O}) \sim \prod_{l=1}^L (|\sin(\theta_l)| + |\cos(\theta_l)|)^2 / M$, leading to an overall sample complexity of $\mathcal{O}\left(\prod_{l=1}^L (|\sin(\theta_l)| + |\cos(\theta_l)|)^2\right)$.

A key property of this decomposition is that, for every parameterized layer $\mathcal{U}_l(\theta_l)$,

$$\mathcal{R}_*(\mathcal{U}_l(\theta_l)) = \mathcal{C}(\mathcal{U}_l(\theta_l)) = |\sin \theta_l| + |\cos \theta_l|, \quad (16)$$

where \mathcal{R}_* denotes the channel robustness and \mathcal{C} the magic capacity. This equality was observed numerically in Ref. [23] and is rigorously proven in Suppl. Mat. II. Equation (16) implies that the single-layer Clifford decomposition already attains the minimal ℓ_1 -norm representation for each parameterized gate. However, obtaining a CSP decomposition of the entire circuit $\mathcal{C}(\theta)$ that minimizes the total ℓ_1 -norm is generally infeasible. Thus, in practical simulations, Static and Dynamic Monte Carlo methods also operate in a layer-wise manner and their resulting sample complexities coincide with that of SPMC.

C. Classical simulation under noise

In realistic quantum hardware, parameterized circuits $\mathcal{C}(\theta)$ are inevitably affected by noise. Recall that we model an imperfectly implemented gate as

$$\tilde{\mathcal{U}}_l(\theta_l) = \mathcal{E}_l \circ \mathcal{U}_l(\theta_l),$$

where \mathcal{E}_l is a noise channel, i.e., a completely positive trace-preserving (CPTP) map. The resulting noisy circuit is denoted by $\tilde{\mathcal{C}}(\theta)$, following the notation introduced in Section II A. For each parameterized rotation gate $\mathcal{U}_l(\theta_l) = e^{-i\theta_l P_l/2} C_l$, we consider a Pauli noise channel aligned with the rotation axis:

$$\mathcal{E}_{P_l}(\rho) = (1 - \gamma_l)\rho + \gamma_l P_l \rho P_l^\dagger, \quad (17)$$

where γ_l is the single-gate noise rate. When the expectation value of a PQC is viewed as a function of its parameters, such axis-aligned Pauli noise suppresses the high-frequency components of the function at an exponential rate with respect to the frequency [46, 47].

In this subsection, we analyze the classical simulation cost of noisy circuits under the above noise model using

the SPMC framework. In our approach, each noisy rotation gate $\tilde{\mathcal{U}}_l(\theta_l)$ is treated as a single composite channel and decomposed directly into a linear combination of Clifford circuit channels, after which quasiprobability Monte Carlo sampling is performed. This is in contrast to a layer-wise treatment in which the noiseless rotation $\mathcal{U}_l(\theta_l)$ and the noise channel \mathcal{E}_l are handled separately. By combining them before decomposition, the resulting ℓ_1 -norm of the coefficients is typically smaller than in the noiseless case, reflecting the fact that noise reduces the non-stabilizerness of the underlying operation [48, 49]. As a consequence, once the noise is sufficiently strong, the Monte Carlo simulation becomes easier: the variance of the estimator decreases and may even approach a constant. Such noise-introduced reductions in simulation cost have been observed numerically for rotation gates under amplitude-damping noise [23], as well as for CCX-type gates subject to depolarizing noise in qudit systems [41]. Here, we characterize this effect for parameterized quantum circuits with axis-aligned Pauli noise and subsequently extend the analysis to general Pauli noise channels.

We consider a noisy rotation gate channel $\mathcal{E}_{P_l} \circ \mathcal{R}_l(\theta_l)$, where $\mathcal{R}_l(\theta_l)$ denotes the unitary rotation channel generated by P_l . For the noise model in Eq. (17), the composite channel simplifies to a mixture of two rotation gate channels:

$$\mathcal{E}_{P_l} \circ \mathcal{R}_l(\theta_l) = (1 - \gamma_l) \mathcal{R}_l(\theta_l) + \gamma_l \mathcal{R}_l(\theta_l + \pi). \quad (18)$$

This channel can be further decomposed into a linear combination of the four Clifford circuit channels $\{\mathcal{R}_l(k\pi/2)\}_{k=0}^3$, with coefficients

$$\begin{aligned} a_0 &= \frac{|\cos \theta_l|}{2(|\sin \theta_l| + |\cos \theta_l|)} + \frac{(1-2\gamma_l)\cos \theta_l}{2}, \\ a_2 &= \frac{|\cos \theta_l|}{2(|\sin \theta_l| + |\cos \theta_l|)} - \frac{(1-2\gamma_l)\cos \theta_l}{2}, \\ a_1 &= \frac{|\sin \theta_l|}{2(|\sin \theta_l| + |\cos \theta_l|)} + \frac{(1-2\gamma_l)\sin \theta_l}{2}, \\ a_3 &= \frac{|\sin \theta_l|}{2(|\sin \theta_l| + |\cos \theta_l|)} - \frac{(1-2\gamma_l)\sin \theta_l}{2}. \end{aligned}$$

The ℓ_1 -norm of this decomposition is

$$\sum_{k=0}^3 |a_k| = \max[1, (1 - 2\gamma_l)(|\sin \theta_l| + |\cos \theta_l|)]. \quad (19)$$

Thus, when

$$(1 - 2\gamma_l)(|\sin \theta_l| + |\cos \theta_l|) \leq 1, \quad (20)$$

the noisy rotation gate becomes a convex combination of Clifford channels.

Consequently, for a noisy circuit $\tilde{\mathcal{C}}(\theta)$ under axis-aligned Pauli noise, the variance of the SPMC estimator for estimating the noisy expectation $\langle O_{\text{noisy}} \rangle = \text{Tr}(O \tilde{\mathcal{C}}(\theta)(\rho))$ scales as

$$\text{Var}(\hat{O}) \sim \frac{\prod_{l=1}^L [\max(1, (1 - 2\gamma_l)(|\sin \theta_l| + |\cos \theta_l|))]^2}{M}, \quad (21)$$

where M is the number of Monte Carlo samples. The corresponding sample complexity is therefore

$$\mathcal{O}\left(\prod_{l=1}^L \max[1, (1 - 2\gamma_l)(|\sin \theta_l| + |\cos \theta_l|)]^2\right). \quad (22)$$

This expression shows that increasing noise monotonically suppresses the non-Clifford contribution to the simulation cost. Beyond the critical noise level

$$\gamma_{c,l} = \frac{1}{2} \left(1 - \frac{1}{|\sin \theta_l| + |\cos \theta_l|}\right), \quad l = 1, 2, \dots, L,$$

each noisy rotation becomes a probabilistic mixture of Clifford operations, and the entire circuit becomes efficiently simulable.

Finally, when the noise model includes additional Pauli components beyond the axis-aligned term in Eq. (17)—for example, the general form in Eq. (4)—the SPMC estimator remains efficiently simulable as long as the axis-aligned component satisfies the condition (20).

In the next section, we demonstrate how noisy quantum hardware can be used to further enhance the efficiency of our SPMC.

IV. LEVERAGING NOISY QUANTUM DEVICES FOR CLASSICAL SIMULATION

A. Motivating observations

Classical simulation of non-Clifford quantum circuits becomes challenging when the ℓ_1 -norm of the Clifford decomposition grows rapidly with circuit depth. However, it turns out that this pessimistic picture can be substantially improved. Before elaborating on how to achieve this, let us present three relevant observations with each revealing a distinct mechanism to alleviate the hardness of simulating a quantum circuit.

Observation 1: Global decompositions and hardware-assisted coefficient learning

Many quantum circuits that appear complex at the gate level may admit surprisingly simple global Clifford decompositions. A prominent example is the multi-controlled- Z gate $C^{n-1}Z$. Although any Clifford+ T implementation of $C^{n-1}Z$ necessarily uses $\Omega(n)$ non-Clifford T gates [50–52]—suggesting an exponentially growing cost if simulated layer by layer via Monte Carlo—recent work has shown that its global magic capacity is bounded by $\mathcal{C}(C^{n-1}Z) < 5$ [49]. Consequently, the optimal Clifford decomposition of the entire gate incurs only a constant simulation cost, independent of n . This illustrates that a circuit containing many non-Clifford components can still be classically tractable once an appropriate global decomposition is identified.

A natural question then arises: *How can one find such low-cost decompositions in practice?* For parameterized rotations, the decomposition coefficients

$$\mathcal{R}_Z(\theta) = \sum_{k=0}^3 a_k \mathcal{R}_Z(k\pi/2)$$

are analytically known, but for deep multi-gate circuits such coefficients are typically inaccessible.

Here, noisy quantum devices offer a useful clue. Consider a realistic device where each $R_Z(\theta)$ gate is followed by a dephasing channel that is independent of θ , as is standard for superconducting qubits due to virtual- Z implementations. Even though the exact noise rate is unknown, one can experimentally obtain coefficients $\{b_k\}$ satisfying

$$\tilde{\mathcal{R}}_Z(\theta) = \sum_{k=0}^3 b_k \tilde{\mathcal{R}}_Z(k\pi/2),$$

by measuring expectation values on hardware. Because the noise channel is the same on both sides, applying its inverse recovers the noiseless decomposition:

$$\mathcal{R}_Z(\theta) = \sum_{k=0}^3 b_k \mathcal{R}_Z(k\pi/2).$$

Thus, the noisy device effectively learns a valid decomposition for the noiseless channel. This illustrates that intrinsic hardware noise, rather than being purely detrimental, can provide valuable information for identifying efficient global decompositions.

Observation 2: Observable-level equivalence reduces simulation complexity

The previous observation assumed that the Clifford decomposition must match the target circuit at the full channel level. Yet this is unnecessarily restrictive: experiments only access expectation values for specific input states and observables. If we relax the requirement and enforce equality only at the level of expectation values,

$$\text{Tr}(O \mathcal{C}(\theta)(\rho)) = \sum_k a_k \text{Tr}(O \mathcal{C}_k(\rho)),$$

the required number of Clifford terms and the associated ℓ_1 -norm can be substantially reduced.

A simple example is the circuit $\mathcal{R}_Z(\theta) \circ \mathcal{H}$ with input $|0\rangle$ and observable X . Channel-level decomposition in Lemma 2 requires four Clifford terms and leads to a cost of $(|\sin \theta| + |\cos \theta|)^2$. However, matching only the observable value allows the single-term choice $a_0 = \cos \theta$, leaving only a single nonzero term. This demonstrates that relaxing to observable-level equivalence can dramatically improve the efficiency of classical simulation.

Observation 3: Restoring transferability via Pauli insertions

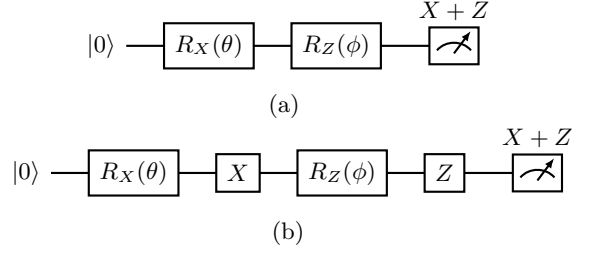


Figure 1: A single-qubit PQC with observable $X + Z$ used in Observation 3.

Observable-level decompositions introduce a subtle challenge: coefficients learned from noisy hardware may fail to reproduce the correct expectation values of the corresponding noiseless circuit—even when the noise is Pauli and independent of the rotation angles. The following example illustrates this issue and a simple remedy.

Consider the circuit in Fig. 1a, where $R_X(\theta)$ and $R_Z(\phi)$ are followed by Pauli noise channels $\mathcal{E}_X(\rho) = (1 - \gamma_1)\rho + \gamma_1 X \rho X$ and $\mathcal{E}_Z(\rho) = (1 - \gamma_2)\rho + \gamma_2 Z \rho Z$, respectively. For input $|0\rangle$ and observable $O = X + Z$, the noisy expectation values are

$$\begin{aligned} \langle X_{\text{noisy}} \rangle &= (1 - 2\gamma_1)(1 - 2\gamma_2) \sin \theta \sin \phi, \\ \langle Z_{\text{noisy}} \rangle &= (1 - 2\gamma_1) \cos \theta, \\ \langle O_{\text{noisy}} \rangle &= (1 - 2\gamma_1)(1 - 2\gamma_2) \sin \theta \sin \phi + (1 - 2\gamma_1) \cos \theta. \end{aligned} \quad (23)$$

In the ideal limit $\gamma_1 = \gamma_2 = 0$, this reduces to $\sin \theta \sin \phi + \cos \theta$.

Following the decomposition in Lemma 2, the noiseless observable satisfies

$$\begin{aligned} &\text{Tr}((X + Z) \mathcal{R}_Z(\phi) \circ \mathcal{R}_X(\theta)(\rho)) \\ &= \sum_{k,l=0}^3 a_{k,l} \text{Tr}((X + Z) \mathcal{R}_Z(l\pi/2) \circ \mathcal{R}_X(k\pi/2)(\rho)). \end{aligned} \quad (24)$$

However, the noisy-device relation becomes

$$\begin{aligned} &\text{Tr}((X + Z) \mathcal{E}_Z \circ \mathcal{R}_Z(\phi) \circ \mathcal{E}_X \circ \mathcal{R}_X(\theta)(\rho)) \\ &= \sum_{k,l=0}^3 a_{k,l} \text{Tr}((X + Z) \mathcal{E}_Z \circ \mathcal{R}_Z(l\pi/2) \circ \mathcal{E}_X \circ \mathcal{R}_X(k\pi/2)(\rho)). \end{aligned} \quad (25)$$

A direct check shows that Eqs. (24) and (25) are generally not equivalent; for example, choosing $a_{0,0} = (1 - 2\gamma_2) \sin \theta \sin \phi + \cos \theta$ and all other $a_{k,l} = 0$ exactly satisfies the noisy relation (25) but violates the noiseless identity (24), so coefficients that fit the noisy data need not reproduce the noiseless expectation value.

To restore transferability, we insert Pauli gates after each rotation, as in Fig. 1b. Writing $\mathcal{X}(\rho) = X \rho X$ and

$\mathcal{Z}(\rho) = Z\rho Z$, the modified noisy observable becomes

$$\begin{aligned}\langle X_{\text{noisy}} \rangle &= (1 - 2\gamma_1)(1 - 2\gamma_2) \sin \theta \sin \phi, \\ \langle Z_{\text{noisy}} \rangle &= -(1 - 2\gamma_1) \cos \theta, \\ \langle O_{\text{noisy}} \rangle &= (1 - 2\gamma_1)(1 - 2\gamma_2) \sin \theta \sin \phi - (1 - 2\gamma_1) \cos \theta.\end{aligned}\quad (26)$$

The corresponding noisy decomposition reads

$$\begin{aligned}\text{Tr}((X + Z)\mathcal{E}_Z \circ \mathcal{Z} \circ \mathcal{R}_Z(\phi) \circ \mathcal{E}_X \circ \mathcal{X} \circ \mathcal{R}_X(\theta)(\rho)) \\ = \sum_{k,l=0}^3 a_{k,l} \text{Tr}((X + Z)\mathcal{E}_Z \circ \mathcal{Z} \circ \mathcal{R}_Z(l\pi/2) \circ \mathcal{E}_X \circ \mathcal{X} \circ \mathcal{R}_X(k\pi/2)(\rho))\end{aligned}\quad (27)$$

Crucially, if $\{a_{k,l}\}$ satisfy both Eq. (27) and Eq. (25), they also satisfy the noiseless identity Eq. (24). Thus Pauli insertions recover the equivalence between noisy and noiseless decompositions, ensuring that coefficients learned on hardware remain valid in the noiseless setting.

This observation highlights that when the Clifford decomposition is constructed only at the observable level, the coefficients obtained from a noisy device may not generalize to the noiseless regime. By inserting appropriate Pauli gates after each rotation, we can re-establish this correspondence and ensure the learned coefficients remain valid.

B. Noisy-device-enhanced classical simulation protocol (NDE-CS)

Building upon these observations, we now present a general protocol that leverages noisy quantum devices to enhance the classical simulation of non-Clifford quantum circuits, which we call noisy-device-enhanced classical simulation (NDE-CS). Recall that any non-Clifford circuit can be expressed as a linear combination of Clifford circuits. However, both the number of resulting Clifford terms and the ℓ_1 -norm of the combination coefficients scale exponentially with the number of non-Clifford gates, making direct classical simulation intractable. The central challenge, therefore, is to identify a sparse Clifford decomposition—one that contains only a small number of nonzero terms—while retaining accuracy. Our protocol addresses this challenge by combining classical preselection with data collected from noisy quantum devices. The procedure consists of two parts: (1) identifying which Clifford circuits should be retained, and (2) estimating the corresponding coefficients of the chosen linear combination. An overview of the protocol is illustrated in Fig. 2.

1. Part I: Selecting the relevant Clifford circuits

Our goal is to estimate the expectation value of a target non-Clifford circuit

$$\mathcal{U}(\theta) = \mathcal{U}_L(\theta_L) \circ \cdots \circ \mathcal{U}_1(\theta_1)$$

with respect to a stabilizer input state ρ and an observable O that is a polynomial-size linear combination of Pauli operators, i.e., $\text{Tr}(O\mathcal{U}(\theta)(\rho))$. Each gate takes the form $\mathcal{U}_l(\theta_l) = e^{-iP_l\theta_l/2}C_l$, where C_l is a Clifford gate and $P_l \in \{I, X, Y, Z\}^{\otimes n}$ is a Pauli operator.

From Eq. (13), we can write

$$\mathcal{U}(\theta) = \sum_{k_1, \dots, k_L} a_{k_1, \dots, k_L} \mathcal{U}_{L, k_L} \circ \cdots \circ \mathcal{U}_{1, k_1}, \quad (28)$$

where $\mathcal{U}_{l, k_l} = \mathcal{U}_l(k_l\pi/2)$ and $k_l \in \{0, 1, 2, 3\}$. The coefficients factorize as $a_{k_1, \dots, k_L} = \prod_{l=1}^L a_{k_l}^{(l)}$, with the optimal single-gate coefficients $a_k^{(l)}$ given in Lemma 2.

Since Eq. (28) involves exponentially many terms, we truncate the expansion by retaining only Clifford circuits associated with large-magnitude coefficients. Let \mathcal{I} denote the index of the retained subset of Clifford circuits. We then approximate

$$\mathcal{U}(\theta) \approx \sum_{(k_1, \dots, k_L) \in \mathcal{I}} b_{k_1, \dots, k_L} \mathcal{U}_{L, k_L} \circ \cdots \circ \mathcal{U}_{1, k_1}. \quad (29)$$

Building on Observation 2, we further relax the requirement that the decomposition hold at the channel level. It suffices for the equality to hold at the observable level:

$$\begin{aligned}\text{Tr}(O\mathcal{U}(\theta)(\rho)) \\ \approx \sum_{(k_1, \dots, k_L) \in \mathcal{I}} b_{k_1, \dots, k_L} \text{Tr}(O\mathcal{U}_{L, k_L} \circ \cdots \circ \mathcal{U}_{1, k_1}(\rho)).\end{aligned}\quad (30)$$

In this setting, certain Clifford circuits may yield zero contribution to the chosen (ρ, O) pair, i.e., $\text{Tr}(O\mathcal{U}_{L, k_L} \circ \cdots \circ \mathcal{U}_{1, k_1}(\rho)) = 0$. These can be safely discarded to further reduce the number of nonzero terms and thus the overall classical simulation cost. Let \mathcal{J} denote the remaining index set of nonzero terms, then our effective approximation becomes

$$\begin{aligned}\text{Tr}(O\mathcal{U}(\theta)(\rho)) \\ \approx \sum_{(k_1, \dots, k_L) \in \mathcal{J}} b_{k_1, \dots, k_L} \text{Tr}(O\mathcal{U}_{L, k_L} \circ \cdots \circ \mathcal{U}_{1, k_1}(\rho)).\end{aligned}\quad (31)$$

In the next part, we describe how to determine the coefficients $\{b_{k_1, \dots, k_L}\}$ using a noisy quantum device.

2. Part II: Estimating the coefficients using a noisy quantum device

Having determined the candidate Clifford circuits (indexed by \mathcal{J}), the remaining task is to compute the coefficients b_{k_1, \dots, k_L} satisfying Eq. (31), which we estimate using data collected from a noisy quantum device.

We assume that each gate $\mathcal{U}_l(\theta_l)$ on hardware is followed by an unknown Pauli noise channel defined in Eq. (4), i.e., $\mathcal{E}_l(\rho) =$

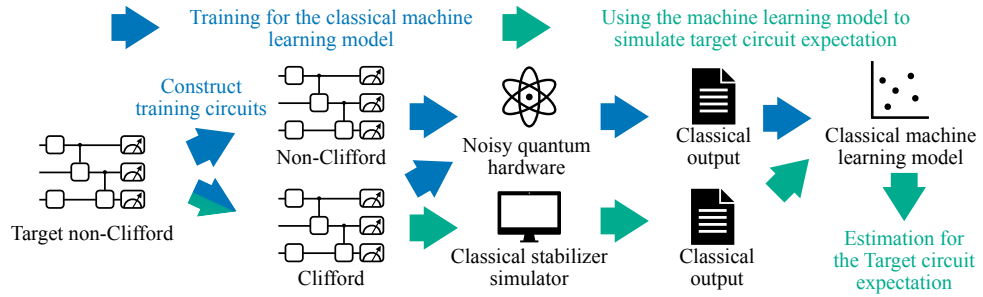


Figure 2: Framework for the NDE-CS protocol. The objective is to estimate the noiseless expectation value of a given observable for a target non-Clifford circuit. The blue arrows indicate the training stage: we construct pairs consisting of the target non-Clifford circuit and associated Clifford circuits. Both types of circuits are run on noisy quantum hardware to obtain measurement data, forming a training dataset for a classical machine-learning model. The model learns a mapping from Clifford-circuit expectations to the corresponding expectations of the target non-Clifford circuit from noisy measurement data. The green arrows denote the inference stage: the trained model takes as input the classically simulated expectations of the Clifford circuits (obtained efficiently via a stabilizer simulator) and outputs a prediction for the target non-Clifford expectation value. Through this framework, noisy quantum devices enhance classical simulation by providing the data needed to learn an effective mapping from Clifford-circuit expectations to target-circuit expectations.

$\bigcup_{k_l \in \mathcal{K}} \left(w_{k_l} \cdot + (1 - w_{k_l}) P_{k_l} \cdot P_{k_l}^\dagger \right) (\rho)$, where the noise distribution $\{w_{k_l}\}$ is independent of the rotation angle θ_l [28, 29]. The noisy circuit channel is then

$$\tilde{\mathcal{U}}(\boldsymbol{\theta}) = \tilde{\mathcal{U}}_L(\theta_L) \circ \cdots \circ \tilde{\mathcal{U}}_1(\theta_1), \quad \tilde{\mathcal{U}}_l(\theta_l) = \mathcal{E}_l \circ \mathcal{U}_l(\theta_l).$$

Naively fitting Eq. (31) on noisy data does not guarantee that the resulting coefficients remain valid for the noiseless circuit, as demonstrated in Observation 3. To address this issue, we employ ‘‘Pauli insertions’’: after each gate $\mathcal{U}_l(\theta_l)$ we insert a randomly selected Pauli gate $\mathcal{P}_l \in \{I, X, Y, Z\}^{\otimes n}$, yielding the modified circuit

$$\mathcal{U}(\boldsymbol{\theta}, \mathbf{P}) = \mathcal{P}_L \circ \mathcal{U}_L(\theta_L) \circ \cdots \circ \mathcal{P}_1 \circ \mathcal{U}_1(\theta_1), \quad (32)$$

and its noisy realization

$$\tilde{\mathcal{U}}(\boldsymbol{\theta}, \mathbf{P}) = \mathcal{P}_L \circ \mathcal{E}_L \circ \mathcal{U}_L(\theta_L) \circ \cdots \circ \mathcal{P}_1 \circ \mathcal{E}_1 \circ \mathcal{U}_1(\theta_1).$$

We then search for coefficients $\{b_{k_1, \dots, k_L}\}$ satisfying

$$\begin{aligned} & \text{Tr} \left(O \tilde{\mathcal{U}}(\boldsymbol{\theta}, \mathbf{P})(\rho) \right) \\ &= \sum_{(k_1, \dots, k_L) \in \mathcal{J}} b_{k_1, \dots, k_L} \text{Tr} \left(O \mathcal{P}_L \circ \tilde{\mathcal{U}}_{L, k_L} \circ \cdots \circ \mathcal{P}_1 \circ \tilde{\mathcal{U}}_{1, k_1}(\rho) \right). \end{aligned} \quad (33)$$

By repeatedly sampling different random insertion patterns \mathbf{P} , we obtain a system of linear equations involving noisy circuit expectations, which can be efficiently measured on hardware. Solving this system on a classical computer yields a set of coefficients $\{b_{k_1, \dots, k_L}\}$ that are theoretically guaranteed to remain valid in the noiseless limit, as shown in Section IV C.

Finally, substituting the obtained coefficients into Eq. (31) and evaluating the Clifford circuit expectations classically (e.g., via stabilizer simulation) provides an es-

timate of the target noiseless expectation value:

$$\langle O \rangle^{(M_C, M_P)} = \sum_{(k_1, \dots, k_L) \in \mathcal{J}} b_{k_1, \dots, k_L} \text{Tr} (O \mathcal{U}_{L, k_L} \circ \cdots \circ \mathcal{U}_{1, k_1}(\rho)). \quad (34)$$

Here, M_C denotes the number of retained Clifford circuits $\{\mathcal{U}_{L, k_L} \circ \cdots \circ \mathcal{U}_{1, k_1}\}_{(k_1, \dots, k_L) \in \mathcal{J}}$, and M_P denotes the number of distinct ‘‘Pauli insertions’’, also referred to as Pauli insertion patterns.

3. Algorithmic summary

Algorithm 1 outlines the complete workflow. The protocol requires $(M_C + 1) \times M_P$ noisy circuit evaluations on hardware and M_C classical Clifford simulations. All noisy evaluations are performed directly on the physical device, and no additional error mitigation or device-specific calibration is required.

Algorithm 1 Noisy-device-enhanced classical simulation protocol

- 1: **Input:** Stabilizer input ρ , observable O , circuit $\mathcal{C}(\boldsymbol{\theta}) = \mathcal{U}_L(\theta_L) \circ \dots \circ \mathcal{U}_1(\theta_1)$, the number of sampled Clifford circuits M_C , and number of Pauli insertion patterns M_P .
- 2: **Output:** Approximate expectation $\langle O \rangle^{(M_C, M_P)} \approx \text{Tr}(O \mathcal{C}(\boldsymbol{\theta})(\rho))$.
- 3: Construct the index set \mathcal{J} of size M_C , where each element $\mathbf{k} = (k_1, \dots, k_L)$ specifies one Clifford configuration $\mathcal{U}_k = \mathcal{U}_L(\frac{k_L \pi}{2}) \circ \dots \circ \mathcal{U}_1(\frac{k_1 \pi}{2})$ with $k_l \in \{0, 1, 2, 3\}$. The configurations are sampled with probability proportional to $|a_k^{(i)}|$ (Eq. (28)) and those with zero observable contribution are discarded.
- 4: **for** $idx = 1$ to M_P **do**
- 5: Randomly select a Pauli insertion pattern $\mathbf{P}^{(idx)} = \{P_1^{(idx)}, \dots, P_L^{(idx)}\}$, where each $P_l^{(idx)} \in \{I, X, Y, Z\}^{\otimes n}$.
- 6: On the noisy hardware, measure a batch of $(M_C + 1)$ expectation values: (i) the target noisy circuit $\text{Tr}(O \tilde{\mathcal{U}}(\boldsymbol{\theta}, \mathbf{P}^{(idx)})(\rho))$, and (ii) for each $\mathbf{k} \in \mathcal{J}$, the basis noisy circuits $\text{Tr}(O \mathcal{P}_L^{(idx)} \circ \tilde{\mathcal{U}}_{L, k_L} \circ \dots \circ \mathcal{P}_1^{(idx)} \circ \tilde{\mathcal{U}}_{1, k_1}(\rho))$.
- 7: These $M_C + 1$ quantities form one linear equation as in Eq. (33). Repeating over M_P random insertion patterns yields a solvable system for $\{b_{\mathbf{k}}\}$.
- 8: **end for**
- 9: Solve the resulting linear system classically for $\{b_{\mathbf{k}}\}_{\mathbf{k} \in \mathcal{J}}$.
- 10: Evaluate each Clifford expectation $\text{Tr}(O \mathcal{U}_{\mathbf{k}}(\rho))$ on a stabilizer simulator.
- 11: Compute $\langle O \rangle^{(M_C, M_P)} = \sum_{\mathbf{k} \in \mathcal{J}} b_{\mathbf{k}} \text{Tr}(O \mathcal{U}_{\mathbf{k}}(\rho))$.
- 12: **return** $\langle O \rangle^{(M_C, M_P)}$.

The algorithm error is quantified by the absolute error ε_{abs} and relative error ε_{rel} , which are defined as follows:

$$\begin{aligned} \varepsilon_{\text{abs}} &= |\langle O \rangle^{(M_C, M_P)} - \text{Tr}(O \mathcal{C}(\boldsymbol{\theta})(\rho))|, \\ \varepsilon_{\text{rel}} &= \frac{|\langle O \rangle^{(M_C, M_P)} - \text{Tr}(O \mathcal{C}(\boldsymbol{\theta})(\rho))|}{|\text{Tr}(O \mathcal{C}(\boldsymbol{\theta})(\rho))|}. \end{aligned} \quad (35)$$

C. Theoretical analysis

In this subsection, we provide theoretical guarantees for the correctness of the proposed protocol, i.e., the coefficients $\{b_{k_1, k_2, \dots, k_L}\}$ learned from noisy circuits with Pauli insertions are valid for reconstructing the noiseless circuit expectation values. The key result is summarized in the following theorem.

Theorem 1 (Effect of Pauli insertions). *Suppose that each noise channel \mathcal{E}_l in the circuit is a Pauli channel, and that its inverse \mathcal{E}_l^{-1} can also be expressed as a linear combination of Pauli channels. If there exist coefficients $\{b_{k_1, k_2, \dots, k_L}\}$ such that, for every choice of Pauli insertions $\mathbf{P} = (\mathcal{P}_1, \dots, \mathcal{P}_L)$ with $\mathcal{P}_l \in \{I, X, Y, Z\}^{\otimes n}$, the corresponding noisy circuit*

$$\tilde{\mathcal{U}}(\boldsymbol{\theta}, \mathbf{P}) = \mathcal{P}_L \circ \mathcal{E}_L \circ \mathcal{U}_L(\theta_L) \circ \dots \circ \mathcal{P}_1 \circ \mathcal{E}_1 \circ \mathcal{U}_1(\theta_1) \quad (36)$$

satisfies

$$\begin{aligned} & \text{Tr}(O \tilde{\mathcal{U}}(\boldsymbol{\theta}, \mathbf{P})(\rho)) \\ &= \sum_{(k_1, \dots, k_L) \in \mathcal{J}} b_{k_1, \dots, k_L} \text{Tr}(O \mathcal{P}_L \circ \tilde{\mathcal{U}}_{L, k_L} \circ \dots \circ \mathcal{P}_1 \circ \tilde{\mathcal{U}}_{1, k_1}(\rho)), \end{aligned} \quad (37)$$

then these coefficients also satisfy the noiseless decomposition relation

$$\begin{aligned} & \text{Tr}(O \mathcal{C}(\boldsymbol{\theta})(\rho)) \\ &= \sum_{(k_1, \dots, k_L) \in \mathcal{J}} b_{k_1, \dots, k_L} \text{Tr}(O \mathcal{U}_{L, k_L} \circ \dots \circ \mathcal{U}_{1, k_1}(\rho)). \end{aligned} \quad (38)$$

Theorem 1 establishes that, under an angle-independent Pauli noise model as defined in Section II A, the coefficients $\{b_{k_1, \dots, k_L}\}$ learned from noisy circuits converge to those yielding the correct noiseless expectation values, provided that the training dataset is sufficiently large. This result guarantees the theoretical soundness of employing noisy quantum hardware to obtain the decomposition coefficients used in our protocol. The proof of Theorem 1 is provided in Suppl. Mat. III.

V. NUMERICAL SIMULATIONS

In this section, we numerically evaluate the performance of the NDE-CS protocol on non-Clifford quantum circuits. We first assess NDE-CS using second-order Trotterized time-evolution circuits of the Ising model, which provide a physically motivated and scalable testbed. Within this circuit model, we then compare NDE-CS with SMC and DMC. Finally, we construct a structured family of circuits to demonstrate a regime in which NDE-CS exhibits a pronounced advantage over SPD, a powerful classical simulation approach that has been shown to successfully simulate quantum circuits at previously inaccessible system sizes.

To numerically simulate noisy quantum hardware outputs, we employ multiple exact simulation methods depending on the qubit number and the circuit type (Clifford or non-Clifford) [53–55].

A. NDE-CS performance on Trotterized circuits

We use second-order Trotterized time-evolution circuits of the Ising model to evaluate the performance of the NDE-CS protocol.

1. Circuit model

The Ising Hamiltonian reads

$$H = - \sum_{\langle i, j \rangle \in E} J_{ij} Z_i Z_j + \sum_i h_i X_i, \quad (39)$$

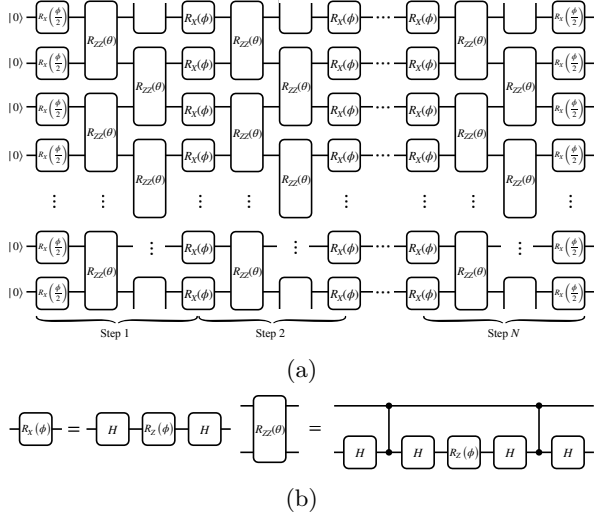


Figure 3: Circuit structure for numerical simulations of the second-order Ising Hamiltonian. (a) The number of qubits is n , and the Trotter step number is N , with $\theta = -\frac{2J_{ij}T}{N}$, $\phi = \frac{2Th_i}{N}$, and the observable $M_Z = \sum_i Z_i$. (b) To mimic realistic superconducting hardware, the rotation gates in (a) are compiled into the native basis consisting of $\{R_Z, CZ, H\}$ gates.

where $\langle i, j \rangle$ denotes a nearest-neighbor pair, $J_{ij} > 0$ is the coupling strength, and h_i represents the transverse field. The time evolution is discretized into N Trotter steps, and the second-order Trotterized propagator is expressed as

$$|\psi(T)\rangle \approx \prod_{k=1}^N \left(\prod_i R_{X_i} \left(\frac{2Th_i}{2N} \right) \prod_{\langle i, j \rangle \in E} R_{Z_i Z_j} \left(-\frac{2J_{ij}T}{N} \right) \prod_i R_{X_i} \left(\frac{2Th_i}{2N} \right) \right) |0\rangle^{\otimes n}. \quad (40)$$

For simplicity, we set $E = \{\langle i, i+1 \rangle : i = 1, \dots, n\}$ with periodic boundary conditions, so that the circuit topology forms a ring, as shown in Fig. 3(a). Each rotation gate is further compiled into the native superconducting gate set $\{R_Z, CZ, H\}$, as illustrated in Fig. 3(b).

In all the simulations, we fix $J_{ij} = 1$, $h_i = -1$, total evolution time $T = 1$, and use the magnetization operator $M_Z = \sum_i Z_i$ as the observable. Different circuit sizes (n qubits) and Trotter steps (N) are explored to test the scalability and accuracy of NDE-CS.

2. Numerical results of NDE-CS

In the noisy simulations, we consider a hardware-inspired Pauli noise model parameterized by γ_X , γ_Y , γ_Z , and γ_{ZZ} . Here, γ_{ZZ} denotes the strength of the two-qubit correlated ZZ noise acting after each two-qubit

gate, while γ_X , γ_Y , and γ_Z represent the single-qubit Pauli error rates associated with X , Y , and Z errors, respectively, which occur independently on both qubits following every two-qubit gate. We set $\gamma_{ZZ} = 10^{-3}$ and $\gamma_X = \gamma_Y = \gamma_Z = 2 \times 10^{-3}$, with enhanced dephasing strength on two-qubit interactions [10, 11]. This configuration enables us to faithfully emulate decoherence and gate imperfections typically present in superconducting quantum processors. Each circuit evaluation uses $N_{\text{shot}} = 2^{14} \approx 1.6 \times 10^4$ measurement shots.

The accuracy of NDE-CS is characterized by both the relative and absolute errors (defined in Eq. (35)). To obtain statistically stable estimates, the protocol is repeated 20 times, and the mean absolute error (MAE) of both the relative and the absolute errors is reported as the final metric.

Fig. 4 illustrates the numerical performance of the NDE-CS protocol for a 16-qubit, 5-step Trotterized Ising circuit $\mathcal{C}(\theta)_{16,5}$. In Fig. 4(a), each point in the color map represents the absolute error ε_{abs} obtained under a specific combination of the number of sampled Clifford circuits M_C (vertical axis) and the number of Pauli insertion patterns M_P (horizontal axis). The corresponding relative error ε_{rel} is shown in Fig. 4(b). Both error metrics exhibit a clear convergence trend as M_C and M_P increase, particularly when M_C exceeds M_P , indicating that the accuracy of NDE-CS systematically improves with richer circuit sampling. Notably, when $M_C \approx 720$ and $M_P \approx 120$, the relative error ε_{rel} drops below 1%, corresponding to a total of $M_{\text{tot}} = (M_C + 1)M_P \approx 8.6 \times 10^4$ noisy circuit evaluations, together with the expectation values of $M_C \approx 720$ Clifford circuits that are computed classically. These results demonstrate that NDE-CS can accurately reconstruct noiseless observable values using only a moderate number of noisy quantum measurements, highlighting its efficiency and practical applicability on near-term hardware.

To further illustrate the convergence behavior, Fig. 4(c) plots the relative error ε_{rel} as a function of M_C for several fixed values of M_P . Each line plot shows a consistent trend of monotonic improvement: for small M_P , the error plateaus early due to insufficient Pauli insertions, while larger M_P values yield faster and smoother convergence with respect to M_C . When both M_C and M_P reach sufficiently large values, the relative error stabilizes below the 1% threshold, confirming the asymptotic convergence of NDE-CS and its robustness against statistical fluctuations in circuit sampling.

B. Comparisons with Static and Dynamic Monte Carlo

We compare our NDE-CS protocol with Static and Dynamic Monte Carlo methods. For the 16-qubit, 5-step Ising circuit $\mathcal{C}(\theta)_{16,5}$, the circuit contains many layers of non-Clifford rotations. To simulate the expectation value of the observable M_Z , Static and Dynamic Monte Carlo

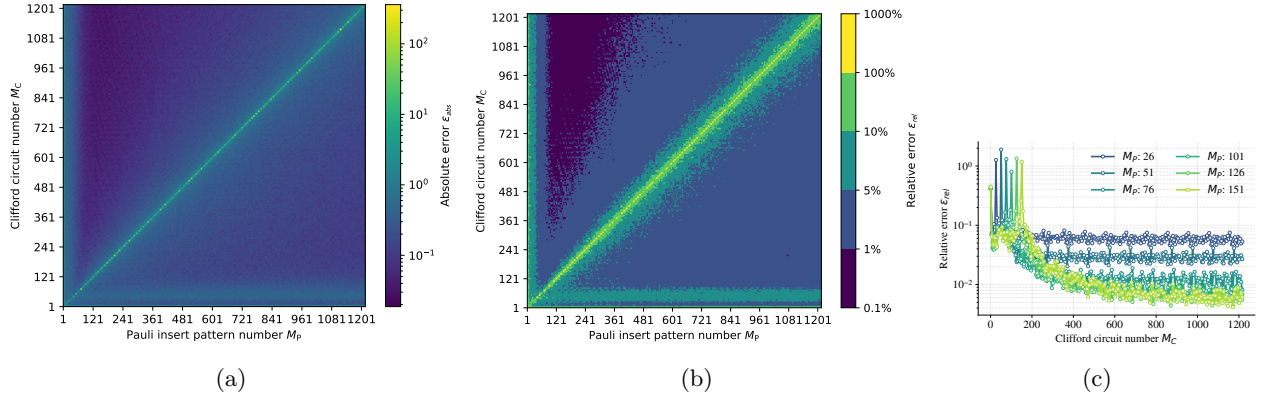


Figure 4: Errors of the NDE-CS protocol for the $n = 16$, $N = 5$ Trotter-step Ising circuit $\mathcal{C}(\theta)_{16,5}$ under different numbers of sampled Clifford circuits M_C and Pauli insertion patterns M_P . (a) Absolute error $\varepsilon_{\text{abs}} = |\langle O \rangle^{(M_C, M_P)} - \text{Tr}(O \mathcal{C}(\theta)(\rho))|$. (b) Relative error $\varepsilon_{\text{rel}} = |\langle O \rangle^{(M_C, M_P)} - \text{Tr}(O \mathcal{C}(\theta)(\rho))| / |\text{Tr}(O \mathcal{C}(\theta)(\rho))|$. The horizontal and vertical axes in (a) and (b) represent M_P and M_C , respectively, and each data point corresponds to the mean of 20 independent NDE-CS runs. Dark-blue regions in (b) correspond to $\varepsilon_{\text{rel}} \leq 1\%$, showing that such (M_C, M_P) configurations are sufficient to achieve sub-percent accuracy in estimating the noiseless expectation. (c) Line plots of the relative error ε_{rel} as a function of M_C for several fixed M_P values. Each curve exhibits monotonic convergence: as both M_C and M_P increase, the relative error systematically decreases and eventually stabilizes below the 1% threshold.

must perform a layer-wise decomposition: each parameterized gate $\mathcal{U}_l(\theta_l)$, $l = 1, \dots, L$, is decomposed independently. From Eq. (16),

$$\mathcal{R}_*(\mathcal{U}_l(\theta_l)) = \mathcal{C}(\mathcal{U}_l(\theta_l)) = |\sin \theta_l| + |\cos \theta_l|. \quad (41)$$

The sample complexities of Static and Dynamic Monte Carlo are both

$$\mathcal{O}\left(\prod_{l=1}^L (|\sin(\theta_l)| + |\cos(\theta_l)|)^2 \varepsilon^{-2}\right), \quad (42)$$

where ε is the target precision. Setting $\varepsilon = 10^{-2}$, the theoretical cost of Static and Dynamic Monte Carlo is approximately $2.46 \times 10^{38} \times 10^4$ samples (up to constants), which is astronomically larger than the number of noisy circuit executions required by NDE-CS (about 8.6×10^4 in Fig. 4).

We also verify this scaling numerically by simulating the Ising circuit $\mathcal{C}(\theta)_{16,5}$ using SMC, as shown in Fig. 5. The figure plots the relative error ε_{rel} as a function of the sample number N_{sample} . Consistent with the theoretical prediction of Eq. (42), the relative error exhibits a clear inverse-square-root relationship, $\varepsilon_{\text{rel}} \propto 1/\sqrt{N_{\text{sample}}}$, demonstrating the characteristic Monte Carlo convergence behavior. By extrapolating the fitted curve, we find that achieving a target precision of 10^{-2} would require approximately 5.29×10^{41} samples—again confirming that the purely classical SMC method incurs an exponentially higher cost than our NDE-CS protocol that leverages noisy quantum hardware.

A complementary comparison is presented in Fig. 6, which compares NDE-CS with SMC and DMC on 10-,

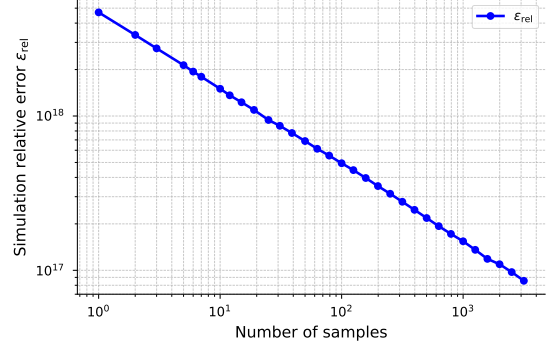


Figure 5: Simulation of the 16-qubit, 5-step Ising circuit $\mathcal{C}(\theta)_{16,5}$ using the SMC method. The figure shows the relation between the number of samples and the simulation relative error ε_{rel} . As illustrated, the relative error decreases proportionally to the inverse square root of the sample number, i.e., $\varepsilon_{\text{rel}} \propto 1/\sqrt{N_{\text{sample}}}$, demonstrating the expected Monte Carlo convergence behavior.

12-, and 14-qubit second-order Trotter circuits over varying Trotter step numbers N . For a target relative error of $\varepsilon_{\text{rel}} = 1\%$, both the number of noisy-hardware shots required by NDE-CS and the number of sampled Clifford circuits required by SMC and DMC increase with circuit depth. However, their growth behaviors differ markedly: the number of Clifford circuits required by SMC and DMC grows essentially exponentially with the number of Trotter steps, whereas the shot complexity of NDE-CS increases much more slowly. Moreover, as the number of qubits increases, the costs of SMC and DMC increase markedly, while the cost of NDE-CS exhibits

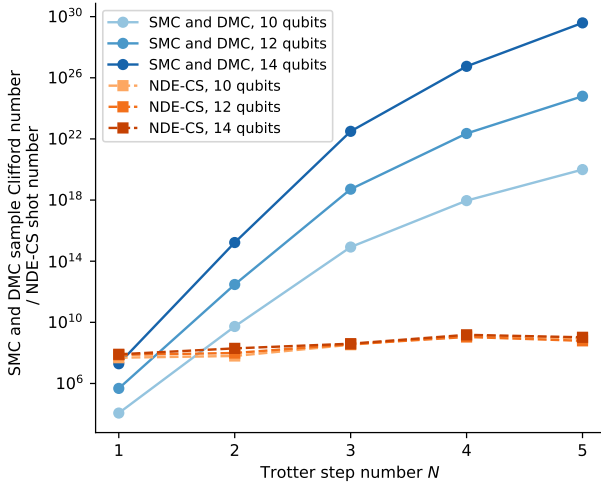


Figure 6: Simulation cost of 10-, 12-, and 14-qubit second-order Trotter circuits for both NDE-CS (red) and SMC as well as DMC (SMC and DMC, blue). The plot shows the number of noisy-hardware shots (NDE-CS) and the number of Clifford circuits (SMC and DMC, defined in Eq. (42)) required to achieve a relative error of $\varepsilon_{\text{rel}} = 1\%$.

only a weak dependence on the system size. This scaling behavior indicates that the advantage of NDE-CS becomes increasingly pronounced for quantum circuits with more qubits.

Although a direct cost equivalence between evaluating a single Clifford circuit expectation and executing a noisy quantum circuit is difficult to establish, Fig. 6 clearly demonstrates that the cost gap between NDE-CS and SMC (and DMC) grows rapidly with increasing circuit depth and qubit number. This separation is expected to become even more pronounced as quantum hardware continues to evolve—with decreasing per-shot cost, increasing qubit counts, and steadily improving gate fidelities—thereby enabling the execution of larger and deeper circuits on noisy devices. Since NDE-CS leverages hardware-executable circuits during its training stage, its effective sampling cost scales favorably with these hardware advances, whereas DMC and SMC face exponentially increasing overhead with a substantially larger prefactor, leading to far steeper scaling than that of NDE-CS even though both methods exhibit exponential behavior. Consequently, the relative advantage of NDE-CS over purely classical simulation methods such as DMC and SMC will continue to strengthen as quantum processors advance toward regimes with significantly more qubits and substantially deeper circuits.

C. Comparisons with Sparse Pauli Dynamics

In recent years, simulation methods based on path-integral formulations have achieved notable progress, sig-

nificantly expanding the class of quantum circuits that can be efficiently simulated on classical hardware [7–9, 55–64]. Among these, the SPD method [55] provides a powerful framework for classically simulating quantum circuits containing a limited number of non-Clifford operations. SPD reformulates the circuit evolution as a deterministic sum over *Pauli paths*, where each path represents a specific sequence of Pauli operators propagating through the circuit. Each Pauli path is associated with a complex amplitude, and the overall circuit dynamics can be approximated by truncating this sum—retaining only the paths with the largest amplitudes while discarding those with negligible contributions. The total number of retained Pauli paths M_{max} therefore directly determines both the computational cost and the achievable accuracy of an SPD simulation. The effectiveness and scalability of SPD have been demonstrated for a variety of practically relevant circuits [58, 60]. In addition, SPD-inspired formulations have recently been leveraged to enhance learning-based quantum error mitigation techniques [65]. These results establish SPD as a representative and competitive classical simulation approach in regimes where the number of non-Clifford operations remains sufficiently limited.

In this subsection, we compare NDE-CS with the SPD method, using the implementation of Ref. [60], with additional methodological details provided in Supplementary Material IV. The specific implementation of SPD introduced in Ref. [60] has been shown to enable converged classical simulations of quantum circuit expectation values at system sizes that were previously beyond the reach of exact methods, including recent large-scale experimental demonstrations [11]. Here, we introduce a structured family of circuits and use it to contrast the scaling behavior of SPD and NDE-CS. For this circuit family, the SPD simulation cost—quantified by the maximum number of Pauli paths M_{max} required to achieve a fixed target accuracy—grows exponentially with the circuit size and depth, whereas the sampling cost of NDE-CS exhibits a markedly weaker dependence on the number of qubits. This establishes a regime where access to noisy quantum hardware provides NDE-CS a clear computational advantage over SPD.

1. A structured circuit family

We first define a controlled- Z gate in the X basis, denoted as CZ_X , as shown in Fig. 7(a). The CZ_X gate is constructed by conjugating a standard CZ gate with Hadamard gates on both qubits, i.e.,

$$\text{CZ}_X := (H \otimes H) \text{CZ} (H \otimes H). \quad (43)$$

For notational clarity in circuit diagrams, we represent CZ_X using blue control nodes and connections, while the standard CZ gate is depicted in black.

We consider a family of circuits acting on an odd num-

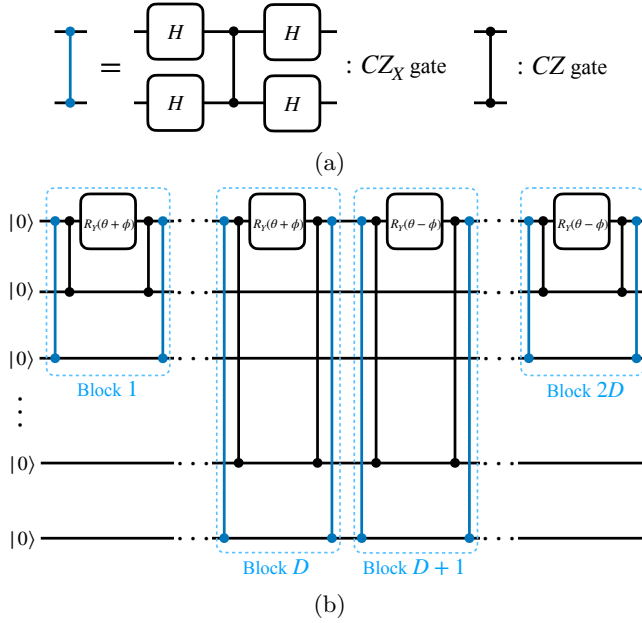


Figure 7: Structured circuit family used to compare NDE-CS with SPD. (a) Definition of the controlled- Z gate in the X basis, $CZ_X = (H \otimes H) CZ (H \otimes H)$. In circuit diagrams, CZ_X is represented using blue control nodes and connections, while the standard CZ gate is shown in black. (b) Circuit architecture on $n = 2D + 1$ qubits composed of $2D$ sequential blocks. The input state is $|0\rangle^{\otimes n}$ and the measured observable is Z_1 .

ber of qubits,

$$n = 2D + 1, \quad D = 1, 2, \dots, \quad (44)$$

with input state $|0\rangle^{\otimes n}$ and the observable Z_1 measured on the first qubit. As illustrated in Fig. 7(b), the circuit consists of $2D$ sequentially arranged blocks. Each block contains two CZ gates, two CZ_X gates, and a single-qubit rotation R_Y , and acts nontrivially only on three qubits. Specifically, within a given block labeled by d , the gate sequence is

$$CZ_X^{(1, 2d+1)} CZ^{(1, 2d)} R_{Y_1}(\theta + \phi) CZ^{(1, 2d)} CZ_X^{(1, 2d+1)}, \quad (45)$$

for $d = 1, 2, \dots, D$, and

$$CZ_X^{(1, 2(2D+1-d)+1)} CZ^{(1, 2(2D+1-d))} R_{Y_1}(\theta - \phi) CZ^{(1, 2(2D+1-d))} CZ_X^{(1, 2(2D+1-d)+1)}, \quad (46)$$

for $d = D+1, D+2, \dots, 2D$. Here, R_{Y_1} denotes a rotation of the first qubit about the Pauli- Y axis, and $CZ^{(i,j)}$ denotes a CZ gate acting on the i -th and j -th qubits (similarly for CZ_X). Notably, the rotation angles of the R_{Y_1} gates differ between the first D blocks and the last D blocks.

We now focus on the parameter choice $\theta = 0$ and $\phi = \pi/4$ in the R_Y gate. In this case, the unitary operations corresponding to the D -th and $(D+1)$ -th blocks

are exact inverses of each other and therefore cancel. The same cancellation occurs between the $(D-1)$ -th and $(D+2)$ -th blocks, and so on, resulting in a complete telescoping cancellation across the circuit. As a consequence, the full circuit unitary is exactly equivalent to the identity operation, and the noiseless expectation value of the observable is $\langle Z_1 \rangle = 1$.

2. Exponential cost of SPD for the structured circuit family

We now analyze the computational cost of simulating this circuit family using SPD. We first consider the case of exact simulation, followed by the more practical setting in which a finite approximation error is allowed.

For exact simulation, no Pauli path can be truncated in the SPD procedure. Numerically, we find that during backward Pauli propagation through the final D blocks of the circuit, the number of Pauli paths doubles after each block. Consequently, after propagating through all D blocks, the total number of Pauli paths reaches 2^D . Moreover, each Pauli path carries an equal weight with magnitude $2^{-D/2}$. As a result, exact simulation requires retaining all 2^D Pauli paths, implying that the computational cost of SPD grows exponentially with D (and hence exponentially with the qubit number $n = 2D + 1$).

We next turn to the more realistic scenario in which a finite simulation error is permitted. We numerically simulate the structured circuit family for $D = 4, 5, \dots, 22$, corresponding to qubit numbers $n = 9, 11, \dots, 45$, and analyze the trade-off between simulation accuracy and the maximum number of retained Pauli paths M_{\max} . The results are summarized in Fig. 8.

Fig. 8(a) shows the relative error ε_{rel} of the SPD simulation as a function of the maximum Pauli path number M_{\max} for different qubit numbers n . For each fixed n , increasing M_{\max} systematically reduces the relative error, as expected. However, as n increases, achieving the same target relative error requires retaining a rapidly growing number of Pauli paths. This exponential scaling is made more explicit in Fig. 8(b), where we plot the Pauli path number required to reach fixed relative error thresholds (80%, 60%, 40%, 10%, and 1%) as a function of the qubit number n . When the Pauli path number M_{\max} is shown on a logarithmic scale, the data exhibit an approximately linear dependence on n , indicating that the required number of Pauli paths grows exponentially with the system size. These results demonstrate that, even when a finite approximation error is allowed, the SPD simulation cost for this circuit family remains exponential in the number of qubits.

3. Performance of NDE-CS for the structured circuit family

We now examine the performance of NDE-CS on the same structured circuit family. We consider circuits with qubit numbers $n = 13, 21, 29$, and 37 . The noise model

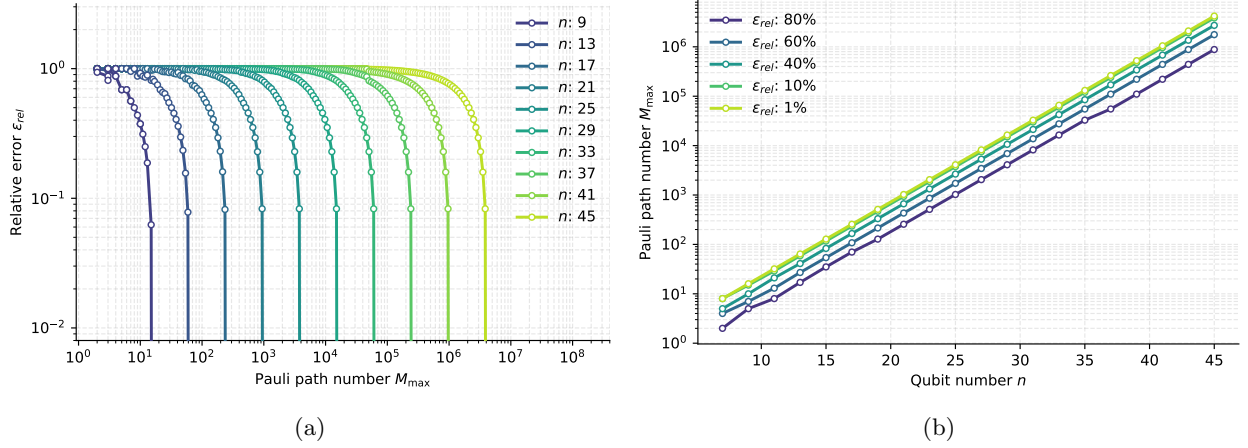


Figure 8: Numerical scaling of SPD for the structured circuit family defined in Fig. 7 with $\theta = 0$ and $\phi = \pi/4$. (a) Relative error ε_{rel} of the SPD simulation as a function of the maximum number of retained Pauli paths M_{max} for different qubit numbers n . (b) Number of Pauli paths required to reach fixed relative error thresholds as a function of the qubit number.

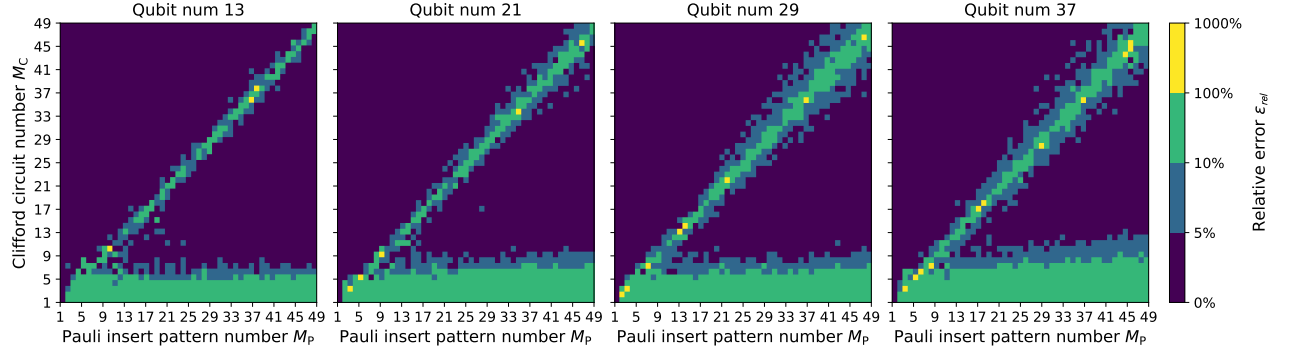


Figure 9: Numerical performance of NDE-CS for the structured circuit family defined in Fig. 7 with $\theta = 0$ and $\phi = \pi/4$. Each panel shows the relative error ε_{rel} between the NDE-CS estimate and the noiseless circuit expectation as a function of the number of sampled Clifford circuits M_C (vertical axis) and the number of Pauli insertion patterns M_P (horizontal axis), for qubit numbers $n = 13, 21, 29$, and 37 . Dark regions correspond to small relative errors, indicating that high accuracy can be achieved with a small number of sampled Clifford circuits and Pauli insertion patterns, even as the system size increases.

used to simulate the noisy quantum circuits is identical to that employed in Section V A 2, and each circuit evaluation uses $N_{\text{shot}} = 2^{14}$ measurement shots. To ensure a nonvanishing training signal, when sampling the Clifford circuits required by NDE-CS we restrict attention to Clifford realizations in which the rotation angles in the d -th and $(2D + 1 - d)$ -th blocks are chosen to be equal for $d = 1, 2, \dots, D$. This constraint guarantees that the corresponding Clifford circuit expectations are nonzero and therefore suitable for training.

For each system size, we evaluate the relative error between the NDE-CS estimate and the noiseless target expectation value as a function of the number of sampled Clifford circuits M_C and the number of Pauli insertion patterns M_P , in close analogy to Fig. 4(b). The results are summarized in Fig. 9. Remarkably, we find that even

with a single sampled Clifford circuit and a single Pauli insertion pattern ($M_C = M_P = 1$), the NDE-CS estimate already achieves relative errors below 5% for all the considered system sizes $n = 13, 21, 29$, and 37 . This behavior stands in clear contrast to SPD, for which the required computational resources grow exponentially with the qubit number for the same circuit family.

Finally, we emphasize that the structured circuit family discussed above is evaluated at the specific parameter point $\theta = 0$ and $\phi = \pi/4$, for which the overall circuit unitary can be reduced to the identity via the cancellation structure described earlier. As a result, the target expectation value can, in principle, be obtained by classical means, even though it cannot be efficiently simulated by SPD due to the exponential growth of Pauli paths. However, we would like to point out that the advantage

of NDE-CS demonstrated here is not restricted to this special case. Indeed, in Suppl. Mat. V, we consider a perturbed setting with $\theta = 0.1$ and $\phi = \pi/4$, where the circuit no longer admits exact cancellation and is not trivially classically simulable, and still observe a similar comparison, indicating that the advantage of NDE-CS over SPD persists for structured non-Clifford circuits with generic rotation angles.

VI. CONCLUSIONS AND DISCUSSIONS

In this work, we develop a framework for the classical simulation of non-Clifford quantum circuits enhanced by noisy quantum circuits. Starting from the SMC formulation [23], we first introduce the SPMC method, which decomposes parameterized quantum circuits into a linear combination of Clifford circuits that retain the same architecture and connectivity as the original circuit. This structure-preserving design guarantees that every sampled trajectory corresponds to a physically consistent circuit, faithfully capturing device-level noise behavior. Although SPMC exhibits an asymptotic sample complexity no smaller than that of the SMC method, it establishes a physically grounded and hardware-compatible foundation for further extensions.

Building upon SPMC, we propose the NDE-CS protocol, which utilizes noisy quantum hardware as a data source to enhance the efficiency of classical simulations. The key idea of NDE-CS is to leverage measurements from noisy Clifford and target circuits to learn coefficients that remain valid for estimating noiseless expectation values. We proved that when the underlying noise model is Pauli and angle-independent, and sufficiently many Pauli insertion patterns are sampled, the coefficients learned from noisy circuits converge to those valid for their noiseless counterparts, thereby enabling accurate classical estimation assisted by real quantum hardware. This insight turns hardware noise from an obstacle into a computational resource.

Numerical simulations on Trotterized Ising circuits demonstrate the strong empirical performance of NDE-CS across a broad range of circuit sizes and depths. While purely classical approaches such as Static and Dynamic Monte Carlo require sample counts that grow rapidly—indeed exponentially—with circuit depth to achieve a given precision, NDE-CS consistently achieves the same relative errors using orders of magnitude fewer samples. For instance, in the 16-qubit, 5-step Trotterized Ising circuit considered in this work, classical Monte Carlo methods require an estimated $\sim 10^{41}$ samples to reach a relative error of 10^{-2} , whereas NDE-CS attains comparable accuracy with only $\sim 10^5$ noisy circuit executions. More generally, our numerical results show that the sampling cost of NDE-CS exhibits a markedly weaker dependence on the qubit number than that of purely classical methods. These findings confirm that combin-

ing noisy quantum data with classical stabilizer simulations can drastically reduce sample complexity without sacrificing estimation accuracy, thereby establishing noise-assisted hybrid computation as a practically advantageous paradigm for simulating large and deep quantum circuits.

In addition to Monte Carlo-based approaches, we further compare NDE-CS with SPD. By constructing a structured family of circuits, we identified a regime in which the computational cost of SPD—quantified by the number of Pauli paths required to reach a fixed accuracy—grows exponentially with the size of the system. In contrast, NDE-CS achieves accurate estimation for the same circuit family with a sampling cost that shows only a weak dependence on the number of qubits. These results highlight a complementary regime in which access to noisy quantum hardware allows NDE-CS to provide a clear practical advantage over purely classical path-based simulation methods.

Beyond the present framework, an exciting future direction is to extend the noisy-device-enhanced paradigm to classical simulators based on tensor networks. In tensor-network simulations, the computational cost typically grows rapidly with the bond dimension, limiting scalability in highly entangled or deep non-Clifford regimes. By incorporating data obtained from noisy quantum hardware—such as reduced density matrices or local observable statistics—one could construct a *noisy-device-enhanced tensor network* approach, where empirical quantum data provide effective priors for tensor truncation or network contraction. Such a hybrid strategy may substantially reduce the simulation cost while maintaining high fidelity, offering a promising route toward large-scale, noise-assisted classical simulation of complex quantum dynamics.

In summary, our work establishes a systematic progression from SMC simulation to SPMC, and finally to the NDE-CS protocol. Together, the SPMC and NDE-CS protocols present a coherent theoretical and practical pathway toward scalable, physically grounded, and noise-resilient quantum-classical simulation frameworks.

Note on Ref. [66]: Just prior to submitting this manuscript to the arXiv, we became aware of the work [66], which presents a similar result to the case where $\theta_l = \pi/4$ for $l = 1, 2, \dots, L$ in Eq. (22) of this manuscript.

ACKNOWLEDGMENTS

We thank Weixiao Sun and Yuguo Shao for valuable discussions. R.Z. and Z.W. were supported by National Natural Science Foundation of China (Grant Nos. 62272259 and 62332009), Beijing Natural Science Foundation (Grant No. Z220002), and Beijing Science and Technology Planning Project (Grant No. Z25110100810000).

[1] P. Shor, Algorithms for quantum computation: Discrete logarithms and factoring, in *Proceedings 35th Annual Symposium on Foundations of Computer Science* (IEEE Comput. Soc. Press, Santa Fe, NM, USA, 1994) pp. 124–134.

[2] S. Lloyd, Universal quantum simulators, *Science* **273**, 1073 (1996).

[3] A. W. Harrow, A. Hassidim, and S. Lloyd, Quantum algorithm for linear systems of equations, *Phys. Rev. Lett.* **103**, 150502 (2009).

[4] P. W. Shor, Polynomial-time algorithms for prime factorization and discrete logarithms on a quantum computer, *SIAM Journal on Computing* **26**, 1484 (1997).

[5] S. Wang, E. Fontana, M. Cerezo, K. Sharma, A. Sone, L. Cincio, and P. J. Coles, Noise-induced barren plateaus in variational quantum algorithms, *Nature Communications* **12**, 6961 (2021).

[6] W. Sun, F. Wei, Y. Shao, and Z. Wei, Sudden death of quantum advantage in correlation generations, *Science Advances* **10**, eadr5002 (2024).

[7] Y. Shao, F. Wei, S. Cheng, and Z. Liu, Simulating Noisy Variational Quantum Algorithms: A Polynomial Approach, *Physical Review Letters* **133**, 120603 (2024).

[8] D. Aharonov, X. Gao, Z. Landau, Y. Liu, and U. Vazirani, A Polynomial-Time Classical Algorithm for Noisy Random Circuit Sampling, in *Proceedings of the 55th Annual ACM Symposium on Theory of Computing* (ACM, Orlando FL USA, 2023) pp. 945–957.

[9] E. Fontana, M. S. Rudolph, R. Duncan, I. Rungger, and C. Cirstoiu, Classical simulations of noisy variational quantum circuits, *npj Quantum Information* **11**, 84 (2025).

[10] E. Van Den Berg, Z. K. Minev, A. Kandala, and K. Temme, Probabilistic error cancellation with sparse Pauli–Lindblad models on noisy quantum processors, *Nature Physics* **19**, 1116 (2023).

[11] Y. Kim, A. Eddins, S. Anand, K. X. Wei, E. Van Den Berg, S. Rosenblatt, H. Nayfeh, Y. Wu, M. Zaletel, K. Temme, and A. Kandala, Evidence for the utility of quantum computing before fault tolerance, *Nature* **618**, 500 (2023).

[12] R. Haghshenas, E. Chertkov, M. Mills, W. Kadow, S.-H. Lin, Y.-H. Chen, C. Cade, I. Niesen, T. Begušić, M. S. Rudolph, C. Cirstoiu, K. Hemery, C. M. Keever, M. Lubasch, E. Granet, C. H. Baldwin, J. P. Bartolotta, M. Bohn, J. Cline, M. DeCross, J. M. Dreiling, C. Foltz, D. Francois, J. P. Gaebler, C. N. Gilbreth, J. Gray, D. Gresh, A. Hall, A. Hankin, A. Hansen, N. Hewitt, R. B. Hutson, M. Iqbal, N. Kotibhaskar, E. Lehman, D. Lucchetti, I. S. Madjarov, K. Mayer, A. R. Milne, S. A. Moses, B. Neyenhuis, G. Park, B. Ponsioen, M. Schecter, P. E. Siegfried, D. T. Stephen, B. G. Tiemann, M. D. Urmy, J. Walker, A. C. Potter, D. Hayes, G. K.-L. Chan, F. Pollmann, M. Knap, H. Dreyer, and M. Foss-Feig, Digital quantum magnetism at the frontier of classical simulations (2025), [arXiv:2503.20870 \[quant-ph\]](https://arxiv.org/abs/2503.20870).

[13] E. Granet, S.-H. Lin, K. Hémery, R. Haghshenas, P. Andres-Martinez, D. T. Stephen, A. Ransford, J. Arkinstall, M. S. Allman, P. Campora, S. F. Cooper, R. D. Delaney, J. M. Dreiling, B. Estey, C. Figgatt, C. Foltz, J. P. Gaebler, A. Hall, A. Husain, A. Isanaka, C. J. Kennedy, N. Kotibhaskar, M. Mills, A. R. Milne, A. J. Park, A. P. Reed, B. Neyenhuis, J. G. Bohnet, M. Foss-Feig, A. C. Potter, R. Nigmatullin, M. Iqbal, and H. Dreyer, Superconducting pairing correlations on a trapped-ion quantum computer (2025), [arXiv:2511.02125 \[quant-ph\]](https://arxiv.org/abs/2511.02125).

[14] F. Alam, J. L. Bosse, I. Čepaité, A. Chapman, L. Clinton, M. Crichigno, E. Crosson, T. Cubitt, C. Derby, O. Dowinton, P. K. Faehrmann, S. Flammia, B. Flynn, F. M. Gambetta, R. García-Patrón, M. Hunter-Gordon, G. Jones, A. Khedkar, J. Klassen, M. Kreshchuk, E. H. McMullan, L. Mineh, A. Montanaro, C. Mora, J. J. L. Morton, D. Patel, P. Rolph, R. A. Santos, J. R. Seddon, E. Sheridan, W. Somogyi, M. Svensson, N. Vaishnav, S. Y. Wang, and G. Wright, Programmable digital quantum simulation of 2D Fermi–Hubbard dynamics using 72 superconducting qubits (2025), [arXiv:2510.26845 \[quant-ph\]](https://arxiv.org/abs/2510.26845).

[15] K. Temme, S. Bravyi, and J. M. Gambetta, Error Mitigation for Short-Depth Quantum Circuits, *Physical Review Letters* **119**, 180509 (2017).

[16] T. Giurgica-Tiron, Y. Hindy, R. LaRose, A. Mari, and W. J. Zeng, Digital zero noise extrapolation for quantum error mitigation, in *2020 IEEE International Conference on Quantum Computing and Engineering (QCE)* (2020) pp. 306–316.

[17] D. Qin, X. Xu, and Y. Li, An overview of quantum error mitigation formulas, *Chinese Physics B* **31**, 090306 (2022).

[18] Z. Cai, R. Babbush, S. C. Benjamin, S. Endo, W. J. Huggins, Y. Li, J. R. McClean, and T. E. O’Brien, Quantum error mitigation, *Reviews of Modern Physics* **95**, 045005 (2023).

[19] S. Guo, J. Sun, H. Qian, M. Gong, Y. Zhang, F. Chen, Y. Ye, Y. Wu, S. Cao, K. Liu, C. Zha, C. Ying, Q. Zhu, H.-L. Huang, Y. Zhao, S. Li, S. Wang, J. Yu, D. Fan, D. Wu, H. Su, H. Deng, H. Rong, Y. Li, K. Zhang, T.-H. Chung, F. Liang, J. Lin, Y. Xu, L. Sun, C. Guo, N. Li, Y.-H. Huo, C.-Z. Peng, C.-Y. Lu, X. Yuan, X. Zhu, and J.-W. Pan, Experimental quantum computational chemistry with optimized unitary coupled cluster ansatz, *Nature Physics* [10.1038/s41567-024-02530-z](https://doi.org/10.1038/s41567-024-02530-z) (2024).

[20] I. L. Markov and Y. Shi, Simulating quantum computation by contracting tensor networks, *SIAM Journal on Computing* **38**, 963–981 (2008).

[21] R. Orús, A practical introduction to tensor networks: Matrix product states and projected entangled pair states, *Annals of Physics* **349**, 117–158 (2014).

[22] S. Bravyi and D. Gosset, Improved Classical Simulation of Quantum Circuits Dominated by Clifford Gates, *Physical Review Letters* **116**, 250501 (2016).

[23] J. R. Seddon and E. T. Campbell, Quantifying magic for multi-qubit operations, *Proceedings of the Royal Society A: Mathematical, Physical and Engineering Sciences* **475**, 20190251 (2019).

[24] J. R. Seddon, B. Regula, H. Pashayan, Y. Ouyang, and E. T. Campbell, Quantifying Quantum Speedups: Improved Classical Simulation From Tighter Magic Monotones, *PRX Quantum* **2**, 010345 (2021).

[25] R. S. Bennink, E. M. Ferragut, T. S. Humble, J. A. Laska, J. J. Nutaro, M. G. Pleszkoch, and R. C. Pooser, Unbi-

ased simulation of near-Clifford quantum circuits, *Physical Review A* **95**, 062337 (2017).

[26] M. Howard and E. Campbell, Application of a Resource Theory for Magic States to Fault-Tolerant Quantum Computing, *Physical Review Letters* **118**, 090501 (2017).

[27] S. Hakkaku and K. Fujii, Comparative Study of Sampling-Based Simulation Costs of Noisy Quantum Circuits, *Physical Review Applied* **15**, 064027 (2021).

[28] P. Krantz, M. Kjaergaard, F. Yan, T. P. Orlando, S. Gustavsson, and W. D. Oliver, A Quantum Engineer’s Guide to Superconducting Qubits, *Applied Physics Reviews* **6**, 021318 (2019).

[29] S. H. Sack and D. J. Egger, Large-scale quantum approximate optimization on non-planar graphs with machine learning noise mitigation, *Physical Review Research* **6**, 013223 (2024).

[30] A. Kandala, A. Mezzacapo, K. Temme, M. Takita, M. Brink, J. M. Chow, and J. M. Gambetta, Hardware-efficient variational quantum eigensolver for small molecules and quantum magnets, *Nature* **549**, 242 (2017).

[31] E. Farhi, J. Goldstone, and S. Gutmann, A Quantum Approximate Optimization Algorithm (2014), [arXiv:1411.4028 \[quant-ph\]](https://arxiv.org/abs/1411.4028).

[32] C. H. Bennett, G. Brassard, S. Popescu, B. Schumacher, J. A. Smolin, and W. K. Wootters, Purification of Noisy Entanglement and Faithful Teleportation via Noisy Channels, *Physical Review Letters* **76**, 722 (1996).

[33] E. Knill, Fault-tolerant postselected quantum computation: Threshold analysis (2004), [arXiv:quant-ph/0404104 \[quant-ph\]](https://arxiv.org/abs/quant-ph/0404104).

[34] O. Kern, G. Alber, and D. L. Shepelyansky, Quantum error correction of coherent errors by randomization, *The European Physical Journal D* **32**, 153–156 (2005).

[35] M. R. Geller and Z. Zhou, Efficient error models for fault-tolerant architectures and the Pauli twirling approximation, *Physical Review A* **88**, 012314 (2013).

[36] J. J. Wallman and J. Emerson, Noise tailoring for scalable quantum computation via randomized compiling, *Physical Review A* **94**, 052325 (2016).

[37] D. Gottesman, Theory of fault-tolerant quantum computation, *Physical Review A* **57**, 127–137 (1998).

[38] S. Aaronson and D. Gottesman, Improved simulation of stabilizer circuits, *Physical Review A* **70**, 052328 (2004).

[39] D. Stahlke, Quantum interference as a resource for quantum speedup, *Physical Review A* **90**, 022302 (2014).

[40] H. Pashayan, J. J. Wallman, and S. D. Bartlett, Estimating outcome probabilities of quantum circuits using quasiprobabilities, *Physical Review Letters* **115**, 070501 (2015).

[41] X. Wang, M. M. Wilde, and Y. Su, Quantifying the magic of quantum channels, *New Journal of Physics* **21**, 103002 (2019).

[42] S. Bravyi, G. Smith, and J. A. Smolin, Trading Classical and Quantum Computational Resources, *Physical Review X* **6**, 021043 (2016).

[43] S. Bravyi, D. Browne, P. Calpin, E. Campbell, D. Gosset, and M. Howard, Simulation of quantum circuits by low-rank stabilizer decompositions, *Quantum* **3**, 181 (2019).

[44] H. Qassim, J. J. Wallman, and J. Emerson, Clifford recompilation for faster classical simulation of quantum circuits, *Quantum* **3**, 170 (2019).

[45] G. Saxena and G. Gour, Quantifying multiqubit magic channels with completely stabilizer-preserving opera-

tions, *Physical Review A* **106**, 042422 (2022).

[46] E. Fontana, M. S. Rudolph, R. Duncan, I. Rungger, and C. Cîrstoiu, Classical simulations of noisy variational quantum circuits, *npj Quantum Information* **11**, 84 (2025).

[47] R. Lu, R. Zhang, W. Li, Z. Wei, D.-L. Deng, and Z. Liu, A unified frequency principle for quantum and classical machine learning (2026), [arXiv:2601.03169 \[quant-ph\]](https://arxiv.org/abs/2601.03169).

[48] F. B. Trigueros and J. A. M. Guzmán, Nonstabilizerness and Error Resilience in Noisy Quantum Circuits (2025), [arXiv:2506.18976 \[quant-ph\]](https://arxiv.org/abs/2506.18976).

[49] F. Wei and Z.-W. Liu, Noise robustness and threshold of many-body quantum magic (2024), [arXiv:2410.21215 \[quant-ph\]](https://arxiv.org/abs/2410.21215).

[50] M. Beverland, E. Campbell, M. Howard, and V. Kliuchnikov, Lower bounds on the non-clifford resources for quantum computations, *Quantum Science and Technology* **5**, 035009 (2020).

[51] J. Jiang and X. Wang, Lower Bound for the T Count Via Unitary Stabilizer Nullity, *Physical Review Applied* **19**, 034052 (2023).

[52] D. Gosset, R. Kothari, and C. Zhang, Multi-qubit Toffoli with exponentially fewer T gates (2025), [arXiv:2510.07223 \[quant-ph\]](https://arxiv.org/abs/2510.07223).

[53] X. Xu, J. Cui, Z. Cui, R. He, Q. Li, X. Li, Y. Lin, J. Liu, W. Liu, J. Lu, *et al.*, Mindspore quantum: A user-friendly, high-performance, and ai-compatible quantum computing framework (2024), [arXiv:2406.17248 \[quant-ph\]](https://arxiv.org/abs/2406.17248).

[54] C. Gidney, Stim: a fast stabilizer circuit simulator, *Quantum* **5**, 497 (2021).

[55] T. Begušić, K. Hejazi, and G. K.-L. Chan, Simulating quantum circuit expectation values by clifford perturbation theory, *The Journal of Chemical Physics* **162**, 154110 (2025).

[56] X. Gao and L. Duan, Efficient classical simulation of noisy quantum computation (2018), [arXiv:1810.03176 \[quant-ph\]](https://arxiv.org/abs/1810.03176).

[57] T. Schuster, C. Yin, X. Gao, and N. Y. Yao, A Polynomial-Time Classical Algorithm for Noisy Quantum Circuits, *Physical Review X* **15**, 041018 (2025).

[58] T. Begušić and G. K.-L. Chan, Real-Time Operator Evolution in Two and Three Dimensions via Sparse Pauli Dynamics, *PRX Quantum* **6**, 020302 (2025).

[59] A. Angrisani, A. Schmidhuber, M. S. Rudolph, M. Cerezo, Z. Holmes, and H.-Y. Huang, Classically Estimating Observables of Noiseless Quantum Circuits, *Physical Review Letters* **135**, 170602 (2025).

[60] T. Begušić, J. Gray, and G. K.-L. Chan, Fast and converged classical simulations of evidence for the utility of quantum computing before fault tolerance, *Science Advances* **10**, eadk4321 (2024).

[61] M. S. Rudolph, E. Fontana, Z. Holmes, and L. Cincio, Classical surrogate simulation of quantum systems with lowesa (2023), [arXiv:2308.09109 \[quant-ph\]](https://arxiv.org/abs/2308.09109).

[62] P. Bermejo, P. Braccia, M. S. Rudolph, Z. Holmes, L. Cincio, and M. Cerezo, Quantum convolutional neural networks are (effectively) classically simulable (2024), [arXiv:2408.12739 \[quant-ph\]](https://arxiv.org/abs/2408.12739).

[63] S. Lerch, R. Puig, M. S. Rudolph, A. Angrisani, T. Jones, M. Cerezo, S. Thanasisip, and Z. Holmes, Efficient quantum-enhanced classical simulation for patches of quantum landscapes (2024), [arXiv:2411.19896 \[quant-ph\]](https://arxiv.org/abs/2411.19896).

- [64] M. S. Rudolph, T. Jones, Y. Teng, A. Angrisani, and Z. Holmes, Pauli Propagation: A Computational Framework for Simulating Quantum Systems (2025), [arXiv:2505.21606 \[quant-ph\]](https://arxiv.org/abs/2505.21606).
- [65] R. Zhang, Y. Shao, F. Wei, S. Cheng, Z. Wei, and Z. Liu, Clifford perturbation approximation for quantum error mitigation, [arXiv:2412.09518](https://arxiv.org/abs/2412.09518) (2024).
- [66] J. Denzler, J. Carrasco, J. Eisert, and T. Guaita, Simulation of noisy quantum circuits using frame representations (2026), [arXiv:2601.05131 \[quant-ph\]](https://arxiv.org/abs/2601.05131).
- [67] A. Heimendahl, M. Heinrich, and D. Gross, The axiomatic and the operational approaches to resource theories of magic do not coincide, [Journal of Mathematical Physics **63**, 112201 \(2022\)](https://doi.org/10.1088/1751-8121/ac6a20).

SUPPLEMENTARY MATERIAL

Supplement Material I: Supplementary Definitions and the Multi-Layer Static Monte Carlo Framework in Section II B

We first provide rigorous definitions of the terms mentioned in Section II B.

Let STAB_n be the set of n -qubit stabilizer states. In an abuse of notation we will use $|\phi\rangle \in \text{STAB}_n$ to mean a pure state from this set, and $\rho \in \text{STAB}_n$ to mean the density matrix of a state taken from the stabilizer polytope, the convex hull of pure stabilizer states. Define $\text{SP}_{n,m}$ to be the set of n -qubit operations \mathcal{E} such that

$$(\mathcal{E} \otimes \mathcal{I}_m)\sigma \in \text{STAB}_{n+m} \quad \text{for all } \sigma \in \text{STAB}_{n+m},$$

where \mathcal{I}_m is the identity map for an m -qubit Hilbert space. The set $\text{SP}_{n,0}$ consists of channels that map n -qubit stabilizer states to n -qubit stabilizer states. We say a channel is completely stabilizer-preserving (CSP) if $\mathcal{E} \in \text{SP}_{n,m}$ for all m . Any CSP channel is necessarily CPTP [67].

A more rigorous definition of $\mathcal{R}_*(\mathcal{E})$ is given by

$$\mathcal{R}_*(\mathcal{E}) = \min_{\Lambda_{\pm} \in \text{SP}_{n,n} \cap \text{CPTP}} \{2p + 1 : (1 + p)\Lambda_+ - p\Lambda_- = \mathcal{E}, p \geq 0\}, \quad (\text{I1})$$

where Λ_{\pm} are completely stabilizer-preserving and CPTP maps. For a CPTP channel \mathcal{E} , the channel robustness satisfies $\mathcal{R}_*(\mathcal{E}) = 1$ if \mathcal{E} is completely stabilizer-preserving, and $\mathcal{R}_*(\mathcal{E}) > 1$ otherwise.

The magic capacity, defined as

$$\mathcal{C}(\mathcal{E}) = \max_{|\phi\rangle \in \text{STAB}_{2n}} \mathcal{R}[(\mathcal{E} \otimes \mathcal{I}_n) |\phi\rangle\langle\phi|], \quad (\text{I2})$$

with \mathcal{I}_n being the identity channel on an n -qubit Hilbert space, and \mathcal{R} the robustness of magic of a quantum state, defined by

$$\mathcal{R}(\rho) = \min_{\vec{q}} \left\{ \|\vec{q}\|_1 : \sum_j q_j |\phi_j\rangle\langle\phi_j| = \rho, |\phi_j\rangle \in \text{STAB}_n \right\}. \quad (\text{I3})$$

Second, we provide the details of the SMC method for general circuits composed of multiple layers. While the main text summarized the overall scaling of the sample complexity as $\mathcal{O}\left(\prod_{l=1}^L \mathcal{R}_*(\mathcal{E}_l)^2\right)$, here we explicitly construct the layer-wise quasiprobability decomposition, define the stabilizer trajectories, and show how unbiased estimators are obtained through sequential sampling.

We begin by expressing each layer \mathcal{E}_l as a linear combination of completely stabilizer-preserving channels,

$$\mathcal{E}_l = \sum_{k_l} q_{k_l}^{(l)} \mathcal{S}_{k_l}^{(l)}, \quad \text{with} \quad \sum_{k_l} q_{k_l}^{(l)} = 1. \quad (\text{I4})$$

Substituting these decompositions into $\mathcal{E} = \mathcal{E}_L \circ \dots \circ \mathcal{E}_1$ yields a sum over all possible stabilizer-preserving trajectories $\vec{k} = (k_1, \dots, k_L)$,

$$\mathcal{E} = \sum_{\vec{k}} \left(\prod_{l=1}^L q_{k_l}^{(l)} \right) (\mathcal{S}_{k_L}^{(L)} \circ \dots \circ \mathcal{S}_{k_1}^{(1)}), \quad (\text{I5})$$

where each trajectory \vec{k} represents one stochastic realization of the circuit evolution.

To estimate the expectation value $\langle O \rangle = \text{Tr}[O \mathcal{E}(\rho)]$, we sequentially sample one stabilizer-preserving map $\mathcal{S}_{k_l}^{(l)}$ from each layer according to

$$p_{\vec{k}} = \frac{\prod_{l=1}^L |q_{k_l}^{(l)}|}{\prod_{l=1}^L \mathcal{R}_*(\mathcal{E}_l)}, \quad s_{\vec{k}} = \prod_{l=1}^L \text{sign}(q_{k_l}^{(l)}).$$

The resulting unbiased Monte Carlo estimator is

$$\hat{O} = \frac{\prod_{l=1}^L \mathcal{R}_*(\mathcal{E}_l)}{M} \sum_{i=1}^M s_{\vec{k}_i} \text{Tr}\left(O \mathcal{S}_{k_L}^{(L)} \circ \dots \circ \mathcal{S}_{k_1}^{(1)}(\rho)\right). \quad (\text{I6})$$

Following the same argument as in the single-layer case, the estimator variance satisfies $\text{Var}(\hat{O}) \sim \prod_{l=1}^L \mathcal{R}_*(\mathcal{E}_l)^2/M$, which leads to the overall sample complexity stated in the main text.

Supplement Material II: Proofs of Lemma 2 and Results in Section III B

In this section, we provide the proof of Lemma 2 and show that

$$\mathcal{R}_*(\mathcal{R}_P(\theta)) = \mathcal{C}(\mathcal{R}_P(\theta)) = |\sin(\theta)| + |\cos(\theta)|,$$

for the Pauli operator $P \in \{I, X, Y, Z\}^{\otimes n}$.

We begin with the case $P = Z_1$, where Z_1 denotes the operator $Z_1 = Z \otimes I \otimes \cdots \otimes I$.

According to the Sandwich Theorem [23], for the channel $\mathcal{R}_{Z_1}(\theta)$, we have

$$\mathcal{R}(\Phi_{\mathcal{R}_{Z_1}(\theta)}) \leq \mathcal{C}(\mathcal{R}_{Z_1}(\theta)) \leq \mathcal{R}_*(\mathcal{R}_{Z_1}(\theta)), \quad (\text{II1})$$

where $\Phi_{\mathcal{R}_{Z_1}(\theta)} := (\mathcal{E} \otimes \mathcal{I})(|\Omega\rangle\langle\Omega|)$, $|\Omega\rangle := \frac{1}{\sqrt{2^n}} \sum_i |ii\rangle$ is the maximally entangled state. Since $\Phi_{\mathcal{R}_{Z_1}(\theta)}$ can be written as the tensor product of $\Phi_{\mathcal{R}_Z(\theta)}$ and $n-1$ Bell states, and Bell states are stabilizer states, tensoring a quantum state with stabilizer states does not change its robustness of magic [26]. Therefore, we have

$$\mathcal{R}(\Phi_{\mathcal{R}_Z(\theta)}) = \mathcal{R}(\Phi_{\mathcal{R}_{Z_1}(\theta)}). \quad (\text{II2})$$

Since $\Phi_{\mathcal{R}_Z(\theta)} = \mathcal{R}_Z(\theta) \cdot \text{CNOT} |+0\rangle\langle+0| \text{CNOT} \cdot \mathcal{R}_Z(\theta)^\dagger = \text{CNOT} \cdot \mathcal{R}_Z(\theta) |+0\rangle\langle+0| \mathcal{R}_Z(\theta)^\dagger \cdot \text{CNOT}$ and the robustness of magic of a single-qubit state with Bloch vector (x, y, z) is given by $\max\{1, |x| + |y| + |z|\}$, we have

$$\mathcal{R}(\Phi_{\mathcal{R}_Z(\theta)}) = \mathcal{R}(\mathcal{R}_Z(\theta) |+0\rangle\langle+0| \mathcal{R}_Z(\theta)^\dagger) = |\cos(\theta)| + |\sin(\theta)| \quad (\text{II3})$$

We now provide a constructive proof that $\mathcal{R}_*(\mathcal{R}_{Z_1}(\theta)) \leq |\cos(\theta)| + |\sin(\theta)|$. It can be directly verified that

$$\mathcal{R}_P(\theta) = \sum_{k=0}^3 a_k \mathcal{R}_P(k\pi/2),$$

where

$$\begin{aligned} a_0 &= \frac{|\cos \theta|}{2(|\sin \theta| + |\cos \theta|)} + \frac{\cos \theta}{2}, & a_2 &= \frac{|\cos \theta|}{2(|\sin \theta| + |\cos \theta|)} - \frac{\cos \theta}{2}, \\ a_1 &= \frac{|\sin \theta|}{2(|\sin \theta| + |\cos \theta|)} + \frac{\sin \theta}{2}, & a_3 &= \frac{|\sin \theta|}{2(|\sin \theta| + |\cos \theta|)} - \frac{\sin \theta}{2}, \end{aligned}$$

and thus $\sum_{k=0}^3 |a_k| = |\cos(\theta)| + |\sin(\theta)|$. By the definition of channel robustness, this implies

$$\mathcal{R}_*(\mathcal{R}_{Z_1}(\theta)) \leq |\cos(\theta)| + |\sin(\theta)|.$$

Combining Eq. (II1), Eq. (II2) and Eq. (II3), we conclude that

$$\mathcal{R}(\Phi_{\mathcal{R}_{Z_1}(\theta)}) = \mathcal{C}(\mathcal{R}_{Z_1}(\theta)) = \mathcal{R}_*(\mathcal{R}_{Z_1}(\theta)) = |\cos(\theta)| + |\sin(\theta)|.$$

For any Pauli operator P , there exists a Clifford gate C such that $CPC^\dagger = Z_1$. By the definitions of channel robustness and magic capacity, and noting that pre- and post-composition of a quantum channel with Clifford gates does not change either the channel robustness or the magic capacity, we obtain

$$\mathcal{R}_*(\mathcal{R}_P(\theta)) = \mathcal{C}(\mathcal{R}_P(\theta)) = |\sin(\theta)| + |\cos(\theta)|.$$

This also completes the proof of Lemma 2.

Supplement Material III: Proofs of Theorem 1

In this section, we provide the detailed proof of Theorem 1. We first rewrite Theorem 1 as follows.

Theorem 2 (Rewrite of Theorem 1). *Suppose that each noise channel \mathcal{E}_i in the circuit is a Pauli channel, and that its inverse \mathcal{E}_i^{-1} can also be expressed as a linear combination of Pauli channels. If there exist coefficients $\{b_{k_1, k_2, \dots, k_L}\}$ such that, for every choice of Pauli insertions $\mathbf{P} = (\mathcal{P}_1, \dots, \mathcal{P}_L)$ with $\mathcal{P}_i \in \{I, X, Y, Z\}^{\otimes n}$, the corresponding noisy circuit*

$$\tilde{\mathcal{U}}(\theta, \mathbf{P}) = \mathcal{P}_L \circ \mathcal{E}_L \circ \mathcal{U}_L(\theta_L) \circ \cdots \circ \mathcal{P}_1 \circ \mathcal{E}_1 \circ \mathcal{U}_1(\theta_1) \quad (\text{III1})$$

satisfies

$$\mathrm{Tr} \left(O \tilde{\mathcal{U}}(\boldsymbol{\theta}, \mathbf{P})(\rho) \right) = \sum_{(k_1, \dots, k_L) \in \mathcal{J}} b_{k_1, \dots, k_L} \mathrm{Tr} \left(O \mathcal{P}_L \circ \tilde{\mathcal{U}}_{L, k_L} \circ \dots \circ \mathcal{P}_1 \circ \tilde{\mathcal{U}}_{1, k_1}(\rho) \right), \quad (\text{III2})$$

then these coefficients also satisfy the noiseless decomposition relation

$$\mathrm{Tr} (O \mathcal{C}(\boldsymbol{\theta})(\rho)) = \sum_{(k_1, \dots, k_L) \in \mathcal{J}} b_{k_1, \dots, k_L} \mathrm{Tr} (O \mathcal{U}_{L, k_L} \circ \dots \circ \mathcal{U}_{1, k_1}(\rho)). \quad (\text{III3})$$

Proof. For each Pauli noise channel \mathcal{E}_i , we assume that its inverse admits the expansion

$$\mathcal{E}_i^{-1} = \sum_{r_i=1}^{R_i} p_{i, r_i} \mathcal{P}_{i, r_i}, \quad \mathcal{P}_{i, r_i}(\rho) = P_{i, r_i} \rho P_{i, r_i}^\dagger, \quad P_{i, r_i} \in \{I, X, Y, Z\}^{\otimes n}. \quad (\text{III4})$$

Using this representation, the noiseless circuit expectation can be rewritten as

$$\begin{aligned} \mathrm{Tr} (O \mathcal{C}(\boldsymbol{\theta})(\rho)) &= \mathrm{Tr} (O \mathcal{U}_L(\theta_L) \circ \dots \circ \mathcal{U}_1(\theta_1)(\rho)) \\ &= \mathrm{Tr} (O \mathcal{E}_L^{-1} \circ \mathcal{E}_L \circ \mathcal{U}_L(\theta_L) \circ \dots \circ \mathcal{E}_1^{-1} \circ \mathcal{E}_1 \circ \mathcal{U}_1(\theta_1)(\rho)) \\ &= \mathrm{Tr} (O \mathcal{E}_L^{-1} \circ \tilde{\mathcal{U}}_L(\theta_L) \circ \dots \circ \mathcal{E}_1^{-1} \circ \tilde{\mathcal{U}}_1(\theta_1)(\rho)) \\ &= \sum_{r_1, \dots, r_L} \left(\prod_{i=1}^L p_{i, r_i} \right) \mathrm{Tr} (O \mathcal{P}_{L, r_L} \circ \tilde{\mathcal{U}}_L(\theta_L) \circ \dots \circ \mathcal{P}_{1, r_1} \circ \tilde{\mathcal{U}}_1(\theta_1)(\rho)). \end{aligned} \quad (\text{III5})$$

By the assumption in Eq. (III2), each noisy circuit term inside the trace can be decomposed as

$$\mathrm{Tr} (O \mathcal{P}_{L, r_L} \circ \tilde{\mathcal{U}}_L(\theta_L) \circ \dots \circ \mathcal{P}_{1, r_1} \circ \tilde{\mathcal{U}}_1(\theta_1)(\rho)) = \sum_{(k_1, \dots, k_L) \in \mathcal{J}} b_{k_1, \dots, k_L} \mathrm{Tr} (O \mathcal{P}_{L, r_L} \circ \tilde{\mathcal{U}}_{L, k_L} \circ \dots \circ \mathcal{P}_{1, r_1} \circ \tilde{\mathcal{U}}_{1, k_1}(\rho)). \quad (\text{III6})$$

Substituting this into the previous expression and rearranging terms gives

$$\begin{aligned} \mathrm{Tr} (O \mathcal{C}(\boldsymbol{\theta})(\rho)) &= \sum_{(k_1, \dots, k_L) \in \mathcal{J}} b_{k_1, \dots, k_L} \sum_{r_1, \dots, r_L} \left(\prod_{i=1}^L p_{i, r_i} \right) \mathrm{Tr} (O \mathcal{P}_{L, r_L} \circ \tilde{\mathcal{U}}_{L, k_L} \circ \dots \circ \mathcal{P}_{1, r_1} \circ \tilde{\mathcal{U}}_{1, k_1}(\rho)) \\ &= \sum_{(k_1, \dots, k_L) \in \mathcal{J}} b_{k_1, \dots, k_L} \mathrm{Tr} (O \mathcal{E}_L^{-1} \circ \tilde{\mathcal{U}}_{L, k_L} \circ \dots \circ \mathcal{E}_1^{-1} \circ \tilde{\mathcal{U}}_{1, k_1}(\rho)) \\ &= \sum_{(k_1, \dots, k_L) \in \mathcal{J}} b_{k_1, \dots, k_L} \mathrm{Tr} (O \mathcal{U}_{L, k_L} \circ \dots \circ \mathcal{U}_{1, k_1}(\rho)), \end{aligned} \quad (\text{III7})$$

which proves Eq. (III3). \square

Supplement Material IV: Methodological Details of SPD

In this appendix, we summarize the SPD method used throughout the main text, which follows the formulation and implementation described in Ref. [60].

Heisenberg-picture formulation

SPD estimates expectation values of observables by propagating operators in the Heisenberg picture. Consider an observable expressed as a linear combination of n -qubit Pauli operators,

$$O = \sum_{Q \in \mathcal{P}} a_Q Q, \quad (\text{IV1})$$

where \mathcal{P} is a subset of the n -qubit Pauli group and $a_Q \in \mathbb{C}$. Each term $a_Q Q$ is referred to as a *Pauli path*, and the coefficient a_Q is called the *weight* of the corresponding Pauli path. For a quantum circuit U , the target expectation value is

$$\langle O \rangle = \langle 0 | U^\dagger O U | 0 \rangle. \quad (\text{IV2})$$

SPD evaluates this quantity by evolving the observable under the adjoint action of the circuit,

$$U^\dagger O U \equiv \mathcal{U}^\dagger(O). \quad (\text{IV3})$$

We consider circuits composed of Clifford gates and Pauli rotation gates of the form

$$U(\theta) := e^{-i\theta P/2} C, \quad (\text{IV4})$$

with P a Pauli operator and C a Clifford gate. Any rotation angle is decomposed as $\theta = \theta' + k\pi/2$, where the Clifford component $k\pi/2$ is absorbed into a Clifford gate and the residual angle satisfies $|\theta'| < \pi/4$.

Pauli path expansion under Pauli rotations

Applying a Pauli rotation gate $U(\theta)$ defined in Eq. (IV4) to an observable O yields

$$U(\theta)^\dagger O U(\theta) = \sum_{Q \in \mathcal{P}'} a'_Q Q, \quad (\text{IV5})$$

where the updated Pauli set is

$$\mathcal{P}' = \{C^\dagger Q C \mid Q \in \mathcal{P}\} \cup \{C^\dagger P Q C \mid Q \in \mathcal{P}, \{P, Q\} = 0\}. \quad (\text{IV6})$$

The coefficients transform as

$$a'_Q = \begin{cases} a_Q \cos \theta + i a_{PQ} \sin \theta, & \{P, Q\} = 0, \\ a_Q, & [P, Q] = 0. \end{cases} \quad (\text{IV7})$$

As a consequence, the number of Pauli terms may increase after each non-Clifford rotation gate $U(\theta)$. In the worst case, repeated Pauli rotations lead to exponential growth of the number of Pauli operators representing the evolved observable.

Truncation and approximate evolution

To obtain a tractable approximation, SPD introduces a truncation operation after each Pauli rotation gate $U_\sigma(\theta)$. Specifically, the Pauli set \mathcal{P}' resulting from the update rule in Eq. (IV5) is truncated after each rotation so as to prevent the number of Pauli paths from growing exponentially with the circuit depth. In the original formulation of SPD [60], only Pauli paths whose weights satisfy $|a_Q| \geq \delta$ are retained for each $Q \in \mathcal{P}'$, where δ is a prescribed truncation threshold.

In our implementation, in order to retain as many Pauli paths as possible while enabling a transparent characterization of the SPD cost, we instead impose a maximum Pauli path number M_{\max} . Whenever the number of Pauli paths in \mathcal{P}' exceeds M_{\max} , the Pauli paths with the smallest weights are discarded. With this scheme, the parameter M_{\max} directly determines the computational cost of the SPD algorithm and serves as the cost metric used throughout the main text.

Supplement Material V: Additional comparisons with SPD

In this section, we provide additional numerical results for the structured circuit family introduced in Section V C, focusing on a parameter regime where exact cancellation does not occur. Specifically, for $\theta = 0.1$ and $\phi = \pi/4$, the circuit no longer admits an exact cancellation of the forward and backward blocks, making it not trivially classically simulable.

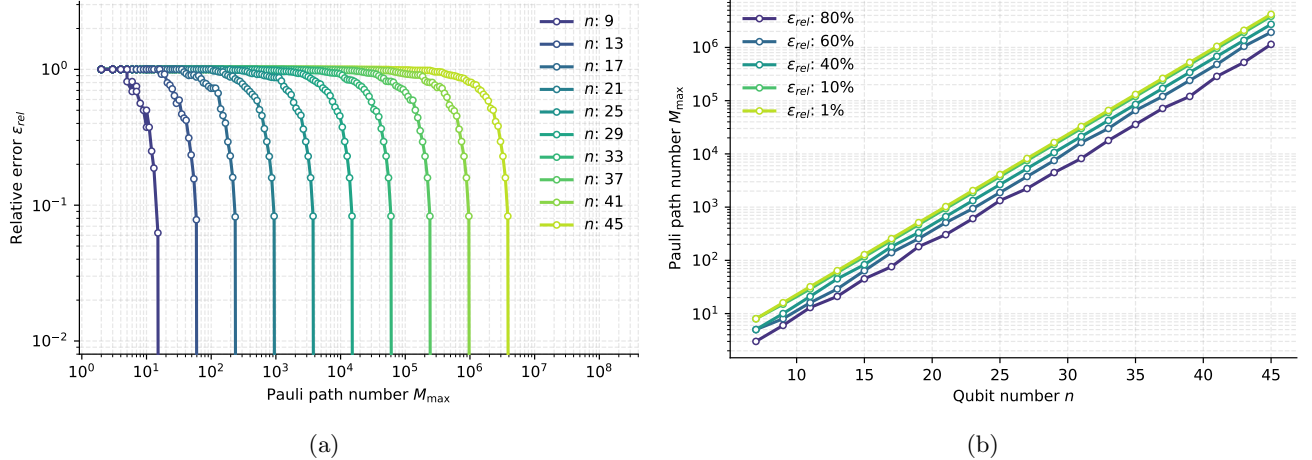


Figure 10: Numerical scaling of SPD for the structured circuit family defined in Fig. 7 with $\theta = 0.1$ and $\phi = \pi/4$. (a) Relative error ε_{rel} of the SPD simulation as a function of the maximum number of retained Pauli paths M_{max} for different qubit numbers n . (b) Number of Pauli paths required to reach fixed relative error thresholds as a function of the qubit number.

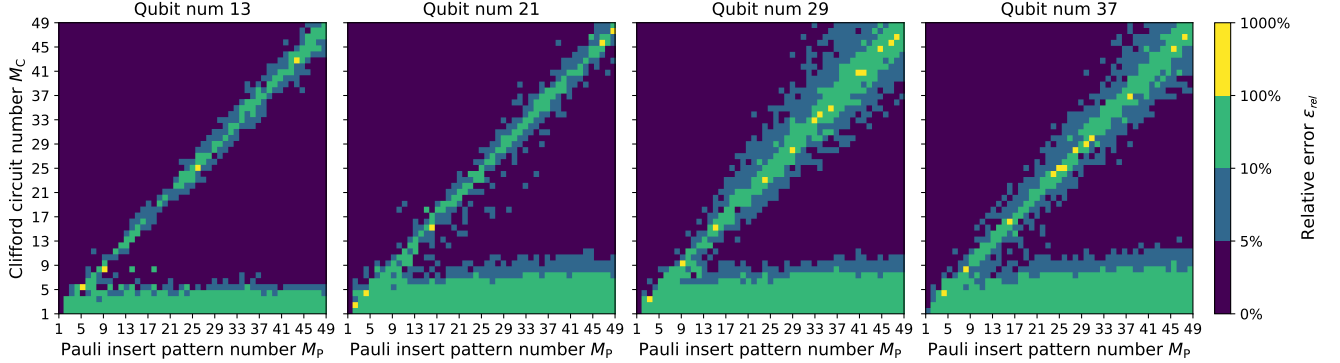


Figure 11: Numerical performance of NDE-CS for the structured circuit family defined in Fig. 7 with $\theta = 0.1$ and $\phi = \pi/4$. Each panel shows the relative error ε_{rel} between the NDE-CS estimate and the noiseless circuit expectation as a function of the number of sampled Clifford circuits M_C (vertical axis) and the number of Pauli insertion patterns M_P (horizontal axis), for qubit numbers $n = 13, 21, 29$, and 37 .

For SPD, consistent with Fig. 8, Fig. 10 shows that the number of Pauli paths required to achieve a fixed target accuracy grows exponentially with the qubit number.

For NDE-CS, Fig. 11 presents the relative error between the NDE-CS estimate and the noiseless circuit expectation as a function of M_C and M_P for qubit numbers $n = 13, 21, 29$, and 37 . Similar to the results obtained at $\theta = 0$ and $\phi = \pi/4$, the NDE-CS estimation error can be reduced below 5% using only a small number of noisy Clifford and noisy target circuit evaluations, and does not exhibit a significant increase with the qubit number over the range considered, in stark contrast to the scaling observed for SPD.